Geometric models for robust encoding of dynamical information into embryonic patterns

Laurent Jutras-Dubé [1], Ezzat El-Sherif [2] *, Paul François [1] *

1 Department of Physics, McGill University, 3600 rue University, H3A 2T8, Montreal, QC, Canada

2 Division of Developmental Biology, Department of Biology, Friedrich-Alexander-Universität Erlangen-Nürnberg, Erlangen 91058, Germany

* Corresponding Authors

Abstract

During development, cells gradually assume specialized fates via changes of transcriptional dynamics, sometimes even within the same developmental stage. For anterior-posterior (AP) patterning in metazoans, it has been suggested that the gradual transition from a dynamic genetic regime to a static one is encoded by different transcriptional modules. In that case, the static regime has an essential role in pattern formation in addition to its maintenance function. In this work, we introduce a geometric approach to study such transition. We exhibit two types of genetic regime transitions, respectively arising through local or global bifurcations. We find that the global bifurcation type is more generic, more robust, and better preserves dynamical information. This could parsimoniously explain common features of metazoan segmentation, such as changes of periods leading to waves of gene expressions, “speed/frequency-gradient” dynamics, and changes of wave patterns. Geometric approaches appear as possible alternatives to gene regulatory networks to understand development.

Introduction

Development from one zygote to a viable animal is a complex process (Wolpert et al., 2006), comprising multiple dynamical sub-processes, including cell movements, tissue morphogenesis, dynamical gene expressions, and cellular differentiations. Eventually, cell identities are fixed by various mechanisms, such as multistable gene regulatory networks and epigenetic markers. Little is known about how this transition from a dynamic/initiation phase to a static/maintenance one is mediated. Are there general characteristics that should be matched between dynamic and static phases to mediate a robust transition?

In dynamical systems theory, a transition between different regimes is called a 'bifurcation', defined as a qualitative change in the dynamics of a system driven by a so-called 'control parameter' (Strogatz, 2015). Bifurcations are of many types but can be systematically classified. For instance, generic families of potentials driving the dynamics have been identified as different "catastrophes" (Poston & Stewart, 2012). While such mathematical descriptions are highly technical, they are reminiscent of the theory of epigenetic landscapes pushed forward by Waddington (Waddington, 1957). It is thus natural to ask if such classifications can be done for development. Could dynamical systems theory help us in this pursuit, and in studying development in general? Here, the main issue is to find a way to frame the problem to derive general results.

In recent years, numerous experimental studies have revealed that quantitative changes of gene expressions during development often followed standard predictions

from dynamical systems theory (Huang et al., 2007). The Waddington landscape's analogy (Jaeger & Monk, 2014) has led to many insights in cell differentiation (Graf & Enver, 2009), and recent data on cell reprogramming quantitatively validated the associated "landscape picture" (Pusuluri et al., 2018). Geometric models of development have been developed in particular cases, precisely predicting the general phenotypes of wildtype and mutants (e.g. the development of *C. elegans* vulva (Corson & Siggia, 2012) and *Drosophila* bristle patterns (Corson et al., 2017)).

The Clock-and-Wavefront model (Cooke & Zeeman, 1976), accounting for the observed dynamical somite (vertebrae precursors) formation, was inspired by catastrophe theory. The model predicted that a retracting wavefront translates the periodic expression of a genetic clock into a spatial pattern via "catastrophic" transitions demarcating the positions of the somites (Figure 1A). Identification of the predicted clock in 1997 (Palmeirim et al., 1997) has since led to many subsequent theoretical and experimental works, including observation of similar clocks in multiple arthropods (El-Sherif et al., 2012; Sarrazin et al., 2012). Cooke and Zeeman originally assumed that the clock is an external process, blind to the subsequent segmentation process it directs (Cooke & Zeeman, 1976). However, it has been very clear from the early experiments in (Palmeirim et al., 1997) that cellular oscillators increase their period prior to segmentation, leading to traveling waves of various signalling pathways such as Notch (Giudicelli et al., 2007; Morelli et al., 2009) (Figure 1A). Importantly, Notch waves eventually stabilize into a pattern of *delta* ligand stripes (Giudicelli & Lewis, 2004; Jiang et al., 2000), with a functional continuity between the dynamic and the static regime. Indeed, it has been shown that the dynamical phase of the clock is encoded into static

rostro-caudal identities (Oginuma et al., 2010). This suggests that the observed oscillation is not a simple external pacemaker for segment formation: rather, clocks, associated waves and the resulting stripes combine into an emergent process leading to proper fate encoding. Segmentation thus possibly appears as the canonical example of transition from a dynamical gene expression regime to a static functional one.

Two broad scenarios have been proposed to model this process (see Figure 1). In the first scenario, the period of the individual oscillators is diverging to infinity as they become more anterior (or similarly, the frequency of the clock is approaching zero), automatically giving rise to a fixed pattern (Figure 1B-F). This model corresponds to Julian Lewis' model for *c-hairy 1* expression pattern in somitogenesis (appendix of (Palmeirim et al., 1997)), and it is possible to experimentally quantify the period divergence within this model (Giudicelli et al., 2007). This also corresponds to the implicit scenario of many theoretical models assuming that the frequency of the clock approaches zero as cells get more anterior, such as the models in (Ares et al., 2012; Morelli & Jülicher, 2007), possibly with a sharp discontinuity suppressing period divergence (Jörg et al., 2015). Those models are appealing owing to their simplicity, since all behaviour is encoded in a dynamical frequency gradient (possibly mediated by FGF (Dubrulle & Pourquié, 2004)). However it is unclear what happens from a dynamical systems theory standpoint (a noteworthy exception being the proposal that the gradient emerges through a singularity in phase similar to the Burger's equation (Murray et al., 2013)). In particular, the pattern in this scenario literally corresponds to a frozen clock, such that there is an infinite number of local steady states corresponding to the frozen phases of the oscillators.

A second scenario grounded in dynamical systems theory has been proposed (François & Siggia, 2012). In this scenario, a genetic network transits from an oscillatory state to an ensemble of (stable) epigenetic states (in Waddington's sense) fixing the pattern. Possible examples include the initial reaction-diffusion based model by Meinhardt (Meinhardt, 1986), or the cell-autonomous model under morphogen control evolved in (François et al., 2007) (Figure 1G). Based on geometric arguments, if bifurcations are local, the most generic model of this transition is expected to present two steps as explained in (François & Siggia, 2012). As a steep control parameter (possibly controlled by a morphogen such as FGF) decreases, the oscillation dies out through a Hopf bifurcation, leading to a single transient intermediate state. Then, for even lower values of the morphogen, one or several new (stable) states appear (technically through saddle-node bifurcations, see Figure 1–figure supplement 1). If the system translates rapidly enough from the oscillatory regime to the multistable regime, a pattern can be fixed (Figure 1H-K). Contrary to the previous scenario where the period of the clock goes to infinity, a Hopf bifurcation is associated to a finite period when the clock stops. The pattern of gene expression itself is laid thanks to multiple expression states discretizing the phase of the clock (Figure 1—figure supplement 1). Importantly, a finite number of states are observed, e.g. anterior and posterior fates within one somite (as first pointed out by Meinhardt (Meinhardt, 1982)).

In this paper, we revisit those ideas with explicit modelling to characterize the behaviour of systems transitioning from a dynamical regime (such as an oscillation) to a static multistable regime. We introduce two new assumptions: 1. the two different phases of developmental expression (dynamic and static) can be separated into two independent

sets of transcriptional modules acting on several genes simultaneously, and 2. the system smoothly switches from one set to the other. This proposal is motivated by the recent suggestion in insects that different sets of enhancers control waves of gap genes at different phases of embryonic growth (El-Sherif & Levine, 2016). Such assumptions explain the so-called “speed-gradient” model suggested to explain the gene expression wave dynamics observed during AP patterning in the beetle *Tribolium* (Zhu et al., 2017) (see Figure 1—figure supplement 2) and (with some additional assumptions) the more subtle gene expression dynamics observed during AP patterning in (Rudolf, Zellner, & El-Sherif, 2020). Using both gene-network and geometric formalisms, we characterize the types of bifurcations found in systems transitioning from a dynamic to a static regime. Surprisingly, we find that if the transition is smooth enough, global bifurcations appear. This situation is different from the standard scenario (Hopf and saddle-nodes) that we nevertheless recover if the transition is more non-linear. This is a generic result that is better studied and understood using geometric models. We further show that the transition through a global bifurcation is more robust than the sequence of Hopf and saddle-node bifurcations with respect to several perturbations that we simulate. Finally, we find that this model can explain many features of metazoan segmentation, such as “speed-gradient” mechanisms or changes of spatial wave profiles due to relaxation-like oscillations, and we discuss biological evidence and implications. This geometric approach thus offers a plausible scenario underlying embryonic patterning with many associated experimental signatures.

Model

In the following, we consider a class of developmental models based on the combination of (at least) two different transcriptional modules. Biologically, those two modules correspond to two sequential developmental phases. The main assumptions are that those transcriptional modules are globally regulated for multiple genes at the same time (which could be done for instance through chromatin global regulations) and that there is a continuous transition from one to the other. Here we focus on metazoan segmentation and regionalization, but the formalism might be applicable to other patterning processes where both an initiation phase and a maintenance phase have been described.

We use ordinary differential equations to model our system. Calling P a vector encoding the state of all proteins in any given cell (typically P corresponds to concentrations of proteins), a generic single-cell equation describing all models presented in the following is:

$$\dot{P} = \theta_D(g)\, D(P) + \theta_S(g)\, S(P) + C(P) + \eta(g, P) \qquad (1)$$

In Eq. 1, variable g encodes an external control parameter of the developmental transition. For example, g could be an external morphogen concentration driving patterning, but more complex situations with feedback are possible, where g could also be part of the system (e.g. the phase difference between oscillators (Beaupeux & François, 2016; Sonnen et al., 2018)). For simplicity, we rescale variables so that g is constrained between 0 and 1. The terms $D(P)$ and $S(P)$ correspond to different sets of modules, their influence on the dynamics being weighted by functions $\theta_D(g)$ and $\theta_S(g)$,

respectively. The term $\eta(g, P)$ encodes the noise. Finally, $C(P)$ represents dynamical terms that are independent of the transcriptional modules, such as protein degradation.

We focus here on the simplest two-module case, where $S(P)$ encodes a multistable system (i.e. with multiple fixed points at steady state) and $D(P)$ a dynamic system (i.e. oscillatory). In this situation we will assume $\theta_S(0) = 1$, $\theta_S(1) = 0$, $\theta_D(0) = 0$, and $\theta_D(1) = 1$, meaning that for $g = 1$ the network is in a pure dynamic phase, while for $g = 0$ the network is multistable. Details on the specific forms of $D(P)$, $S(P)$, $\theta_D(g)$ and $\theta_S(g)$ are given in the following and in the Appendix. We study two types of models: gene-network like models where $D(P)$ and $S(P)$ explicitly model biochemical interactions between genes (such as transcriptional repression), and geometric models where $D(P)$ and $S(P)$ directly encode flows in an abstract 2D phase space, similarly to (Corson & Siggia, 2017).

We model an embryo as a line of cells, corresponding to the antero-posterior axis. The dynamics within each cell (position x) is described by Eq. 1. The only difference between cells is that the dynamics of g is a prescribed function of x, e.g. we assume that there is a function $g(x, t)$ describing the dynamics of a morphogen. We focus on the transition between the two regimes as g continuously changes from 1 to 0 in different cells as a function of time. We will typically consider a sliding morphogen gradient moving along the antero-posterior axis with speed v, described by $H(s(x - vt))$ where the function H encodes the shape of the morphogen, and parameter s is a measure of the gradient's spatial steepness.

We also include noise in the system with the help of an additive Gaussian white noise. For gene networks, we follow an approach similar to the τ-leaping algorithm (Gillespie, 2001), where the variance of the noise corresponds to the sum of the production and the degradation terms (approximating independent Poisson noises). A multiplicative noise intensity term $\sqrt{1/\Omega}$ is introduced, where Ω can be interpreted as the typical concentration of the proteins in the system, so that bigger Ω corresponds to lower noise. In addition, we add diffusion coupling the cells in the stochastic gene network models. For the geometric model, the variance of the noise is held independent of the position x. A more detailed description of the noise and diffusion terms is provided in the Appendix.

All source codes and data used for this paper are available at :
https://github.com/laurentjutrasdube/Dual-Regime_Geometry_for_Embryonic_Patterning

Relation to existing biological networks

The model described above aims at being generic, but one can relate it to existing developmental networks. A two modules dichotomy was initially proposed in the *Drosophila* context, where two enhancers (early and late) were observed for *Krüppel* and *knirps (*E. El-Sherif & Levine, 2016*)*. An extension of this model has been proposed in (Zhu et al., 2017) for a gap gene cascade under control of the maternal gene *Caudal*, which would thus play the role of g (a detailed model is reproduced in the Supplement, see Figure 1—figure supplement 2). The dynamic module corresponds to a genetic cascade comprising *hunchback, Krüppel, mille-pates,* and *giant.* Each gene in this

sequence activates the next one, and later genes repress earlier ones. For the static module, each gene self-activates, and *hunchback* and *Krüppel* repress one another. The situation is less clear for vertebrates, given the plethora of oscillating genes and possible redundancy in three different pathways, specifically *Notch, Wnt* and *FGF* (Dequeant et al., 2006). The two-module system we consider assumes both the dynamic and static regimes are realized by the same set of genetic components (genes and/or signalling pathways). *Notch* signalling is an ideal candidate to be a component of both a dynamic and a static regime that might mediate vertebrate somitogenesis, since Notch is implicated in both the core segmentation clock of vertebrates (e.g. via *Lfng* (Dale et al., 2003), or the *hes/her* family in zebrafish (Lewis, 2003)) and oscillation stabilization (Jiang et al., 2000; Oginuma et al., 2010). Importantly, several genes of the Notch signalling pathways (e.g. *DeltaC* in zebrafish) are first expressed in an oscillatory manner then stabilize in striped patterns, as expected in our model (F. Giudicelli & Lewis, 2004; Wright et al., 2011). There are also multiple genetic interactions between members of the *Notch* pathway, in particular again *Delta* genes (Schwendinger-Schreck, Kang, & Holley, 2014) , with different roles and changes of regulations in the dynamic vs static phase (see e.g. (Wright et al., 2011)).The oscillation itself could be mediated through one or several negative feedback loops in this pathway (Lewis, 2003), and stabilization could be realized through one of the multiple *Notch* signalling interactions (possibly via cell coupling, similarly to what is observed in other systems (Corson, Couturier, Rouault, Mazouni, & Schweisguth, 2017)).

Results

A model for the transition between two genetic modules: Hopf vs. SNIC.

In (Zhu et al., 2017), it was suggested that the transition from a “wave-like” behaviour to a static pattern during *Tribolium* segmentation was mediated by a smooth transition from one set of modules (corresponding to the oscillatory phase) towards another (corresponding to the fixed pattern). This explained the “speed-gradient” mechanism where the typical time-scale of the dynamical system depends strongly on an external gradient (in this case the concentration of the transcription factor *Caudal*). In the Appendix, we further study the associated bifurcation, and observe that new fixed points corresponding to the stabilization of gap gene expressions appear on the dynamical trajectory of those gap genes (Figure 1—figure supplement 2F). In simple words, the gap gene expression pattern slowly “freezes” without any clear discontinuity in its behaviour from the dynamic to the static phase, which is reminiscent of the “infinite-period” scenario displayed on Figure 1.

We first aim to generalize this observed property. A simple way to generate waves of gene expressions (as in the gap-gene system described above) is to consider an oscillatory process, so that each wave of the oscillation corresponds to a wave of gap genes. We are not saying here that the gap-gene system is an oscillator, but rather that its dynamics can be encompassed into a bigger oscillator (Verd et al., 2018)). The other advantage of considering oscillators is that we can better leverage dynamical systems theory to identify and study the bifurcations. Furthermore, it allows for a better connection with oscillatory segmentation processes in vertebrates and arthropods.

We thus start with an idealized gene regulatory network with 3 genes under the control of two regulatory modules (Figure 2). In the dynamic phase $D(P)$, we assume that the 3 genes are oscillating with a repressilator dynamics (Elowitz & Leibler, 2000), so that the system keeps a reference dynamical attractor and an associated period. In the static phase $S(P)$, we assume that the module encodes a tristable system via mutual repression (Figure 2A).

We study the dynamics in a simulated embryo under the control of a regressing front of g (Figure 2B). Transition from the dynamic module to the static module is expected to form a pattern by translating the phase of the oscillator into different fates, implementing a clock and wavefront process similar in spirit to the one in (François et al., 2007). We compare two versions of this model, presenting the two different behaviours that we found. In Model 1 (Figure 2C-H), the weights of the two modules are non-linear in g: $\theta_D(g) = g^2$ and $\theta_S(g) = (1-g)^2$ (Figure 2C). In Model 2 (Figure 2I-N), the weights of the two modules are linear in g: $\theta_D(g) = g$ and $\theta_S(g) = 1-g$ (Figure 2I). We note that the initial and final attractors of both models are identical. Importantly, only the ***transition*** from one set of modules (and thus one type of dynamics) to the other is different. This two-module system thus offers a convenient way to compare the performance of different modes of developmental transition while keeping the same "boundary conditions" (i.e. the same initial and final attractors).

Figure 2E and Figure 2K show the kymographs for both models without noise, with behaviours of individual cells in Figure 2D and Figure 2J. While the final patterns of both models are the same (Figure 2F and Figure 2L), giving rise to a repeated sequence of three different fates, it is visually clear that the pattern formed with Model 2 is more

precise and sharper along the *entire dynamical trajectory* than the one formed with Model 1, which goes through a “blurry” transitory phase (compare mid-range values of g on Figure 2E and Figure 2K).

To better understand this result, we plot the bifurcation diagram of both models as a function of g in Figure 2G and Figure 2M. As g decreases, Model 1 is the standard case of a local Hopf bifurcation (Strogatz, 2015), which happens at $g = 0.72$. Three simultaneous saddle-node bifurcations appear for lower values of g, corresponding to the appearance of the fixed points defining the three regions of the pattern. The behaviour of Model 2 is very different: the fixed points form on the dynamical trajectory, via three simultaneous Saddle Node on Invariant Cycle (or SNIC) bifurcations (Strogatz, 2015). Both models display waves corresponding to the slowing down of the oscillators, leading to a static regime. In Model 1, the time-scale disappears with a finite value because of the Hopf bifurcation (Figure 2H). For Model 2, it diverges because of the SNIC (Figure 2N), suggesting an explicit mechanism for the infinite-period scenario of Figure 1.

To further quantify the differences of performance between the two models, we introduce noise (encoded with variable Ω, see the Model section and the Appendix) and diffusion (Figure 3A-D). We also define a mutual information metric measuring how precisely the phase of the oscillator is read to form the final pattern (Figure 3E, see the Appendix for details), consistent with the experimental observation in vertebrate segmentation that oscillatory phases and pattern are functionally connected (Oginuma et al., 2010). Intuitively, this metric quantifies in a continuous way the number of fates encoded by the system at steady state. Ideal mutual information for the three mutually

exclusive genes of Models 1 and 2 gives $log(3) \sim 1.6$ bits of mutual information, meaning that the pattern deterministically encodes the phase of the cycle into three static fates with equal weights. While addition of noise decreases this mutual information as expected (Figure 3E), Model 2 (black curves) always outperforms Model 1 (red curves). For a reasonable level of noise corresponding to a few thousands of proteins in the system, Model 2 can encode $2^{1.3} \sim 2.5$ fates, close to the optimum 3. Furthermore, for a given diffusion constant, Model 1 requires a ten times smaller noise level than Model 2 to encode the same amount of mutual information, which thus indicates much better noise resistance for Model 2.

Those observations suggest that appearance of stable fixed points through SNIC bifurcations rather than through Hopf bifurcations generates a more robust pattern. The superiority of Model 2 can be rationalized in the following way: when there is a Hopf bifurcation, only one fixed point exists for a range of g values, so that all trajectories are attracted towards it. This corresponds to the “blurred” zone in the kymographs of Figure 2 and Figure 3. In presence of noise, the effect is to partially erase the memory of the phase of the oscillation when only one fixed point is present for the dynamics. Conversely, a SNIC bifurcation directly translates the phase of the oscillation into fixed points, without any erasure of phase memory, ensuring higher information transfer from the dynamic to the static phase, and therefore more precise patterning.

The Hopf bifurcation of Model 1 occurs when the weights of the dynamic and static modules become small compared to the degradation term, which generates an “intermediate regime” with one single fixed point after the oscillations of the dynamic module and before the multistability of the static module. The specific form of the

weights is not what determines the bifurcation, but rather the presence or absence of an intermediate regime. We confirm this observation with similar 3-gene models that used Hill functions for the weights θ_D and θ_S (Figure 2—figure supplement 1 and Figure 3—figure supplement 1). Interestingly, we get both Hopf and SNIC bifurcations with the same shape for the two weights; the Hopf is obtained by shifting the weight of the dynamic term towards larger values of the control parameter. This effectively generates the required intermediate regime where both weights are small compared to the degradation term.

Gene-free models present a similar geometry of transition

Hopf and saddle-node bifurcations are “local” bifurcations, in the sense that changes of the flow in phase space are confined to an arbitrarily small region of phase space as the bifurcation is approached. They do not in principle require complex changes of the flow or fine-tuning of the parameters to happen. As such, they are the most standard cases in many natural phenomena and in most theoretical studies. Conversely, SNIC bifurcations are “global” bifurcations (Strogatz, 2015) (Ermentrout, 2008): they are associated to changes of the flow in large regions of phase space (e.g. when a limit cycle disappears with a non-zero amplitude) and usually require some special symmetries or parameter adjustments to occur (e.g. to ensure that a saddle-node collides with a cycle).

It is therefore a surprise that SNIC bifurcations spontaneously appear in the models considered here. To better understand how this is possible and if this is a generic

phenomenon, we follow ideas first proposed by Corson and Siggia (Corson & Siggia, 2012) and consider geometric (or gene-free) systems. We aim to see if: 1. SNIC bifurcations are generically observed, and 2. a model undergoing a SNIC bifurcation is in general more robust to perturbations than a model undergoing a Hopf bifurcation, with initial and final attractors being held fixed. We thus build 2D geometric versions of the system (variables y and z). The dynamic module $D(P)$ is defined by a non-harmonic oscillator on the unit circle, while the static module $S(P)$ is defined by two stable fixed points, at $y = \pm 1$, $z = 0$ (see Figure 4A, and the Appendix for the equations). Like previously, we build a linear interpolation between the two systems as a function of g and explore the consequence on the bifurcations (Figure 4B-H). Since the flow in the system is 2D, we can also easily visualize it (Figure 4I and Figure 4—movie supplement 2).

In brief, this geometric approach confirms all the observations made on the gene network model of the previous section, and further clarifies the origin of the SNIC bifurcation. Because of the smooth transition between modules, the entire flow in 2D needs to interpolate from a cycle to a bistable situation. When both modules have close to equal weights (around $g = 0.5$), the flow and associated cycle concentrate around two future fixed points. This appears in retrospect as the most natural way to interpolate between the two situations since both types of attractor (stable limit cycle, and multiple stable fixed points) are effectively present at the same time around $g = 0.5$. For this reason, the oscillations are also more similar to relaxation oscillations, rapidly jumping between two values corresponding to the future fixed points. When g is further lowered,

the weight of the static module dominates and “tears apart” the cycle, forming two fixed points.

This situation is so generic that in fact, to obtain a Hopf bifurcation, we need to mathematically reinforce the fixed point at $y = 0$ for intermediate values of g. More precisely, three things are required to get a Hopf bifurcation. First, we need to add an extra term, the “intermediate module”, characterized by a single fixed point at $y = 0$ and $z = 0$. Without this module, we consistently get a SNIC bifurcation, for all forms of coupling tested, including linear and non-linear couplings (Figure 4—figure supplement 1A-D). Second, we need to set the weight of the intermediate module to 0 for $g = 1$ and $g = 0$, so that we get the oscillations of the dynamic module at the beginning of the simulation and the bistability of the static module at the end of the simulation. We achieve this by setting the weight of the intermediate term to $g(1 - g)$, which is of 2nd order in g. Third, we need to make the weights of the dynamic and static modules smaller than the weight of the intermediate module for intermediate values of the control parameter, i.e. for g around 0.5. This is achieved by using cubic weights for the dynamic and static modules (Figure 4—figure supplement 1G and Figure 4—figure supplement 2). Weights of the 4th order in g also lead to a Hopf bifurcation (Figure 4—figure supplement 1H), while linear weights lead to a SNIC bifurcation (Figure 4—figure supplement 1E). Interestingly, quadratic weights lead to simultaneous supercritical Hopf and pitchfork bifurcations (Figure 4—figure supplement 1F). The non-linearity of the coupling helps reinforce the relative weight of the intermediate module for values of g around 0.5, but the exact shape of the non-linearity is not crucial. Furthermore, our mutual information metric confirms that the pattern is more robustly encoded when the

system goes through a SNIC bifurcation rather than through a sequence of Hopf and pitchfork bifurcations (Figure 4—figure supplement 5F).

Detailed simulations of the gene-free model with the intermediate module and with cubic weights for the dynamic and static modules are shown on Figure 4—figure supplement 2. As expected for a Hopf bifurcation, the flow first concentrates on the central fixed point at $y = 0$, before re-emerging in a bistable pattern for lower g (Figure 4—figure supplement 2I and Figure 4—movie supplement 1). There are technically two types of Hopf bifurcations, depending on the stability of the limit cycle. A Hopf bifurcation is supercritical (resp. subcritical) if a stable (resp. unstable) limit cycle becomes a stable (resp. unstable) fixed point. All Hopf bifurcations discussed previously are supercritical. However, by changing slightly the dynamic module of the gene-free model (and including the intermediate module as well as cubic weights for the dynamic and static modules) we can also obtain a subcritical Hopf bifurcation (Figure 4—figure supplement 3). During this bifurcation, an unstable limit cycle forms around the origin. This unstable limit cycle coexists with the stable limit cycle of the dynamic module for some range of g values before they annihilate each other during a so-called “saddle-node of limit cycles” bifurcation. Finally, the two fixed points of the static module form during two simultaneous saddle-node (of fixed points) bifurcations (Figure 4—figure supplement 3I and Figure 4—movie supplement 3). Again, our mutual information metric confirms that the pattern is more precise when the system goes through a SNIC bifurcation (Model 2), rather than through supercritical or subcritical Hopf bifurcations (Models 1 and 3, resp.) (Figure 4—figure supplement 5E). Taken together, these results suggest that keeping the static and dynamic attractors fixed, patterning is both more generic and more

robustly encoded through a SNIC bifurcation than through a Hopf bifurcation, at least in simple low-dimension models.

Robustness and asymmetry in the fixed points

A concern with the results of the previous section might be that those mathematical models are in fact fine-tuned and too symmetrical, so that in particular when the transition occurs, both new fixed points appear for the same value of the control parameter. Furthermore, real biological networks have no reason to be perfectly symmetrical (although evolution itself might select for more symmetrical dynamics if needed). We thus relax our hypotheses to study a system where parameters and trajectories are not symmetrical (Figures 5 and 6).

Going back first to the gene network model, we induce an asymmetry between the fixed points by changing thresholds of repression in the static phase (Figure 5A). The bifurcation diagrams of Figure 5B-C indicate that the asymmetry of the fixed points indeed breaks the simultaneity of appearance of all fixed points in both scenarios. We nevertheless notice that for those changes of parameters, all bifurcations still happen in a very narrow range of g for the SNIC model.

Asymmetry of the fixed points might therefore destroy the advantage of SNIC vs Hopf by creating a transient zone where one of the fixed points always dominates. We thus perform a comparison between Models 1 and 2 with the same asymmetric static enhancers (Figure 5, see also Figure 5—figure supplements 1 and 2, and the Appendix for details). To compare the two cases, we consider different time-scales of the

morphogen gradient. The reasoning is that the slower the decay of g, the more time the system spends in a region of parameter space without all three final fixed points, allowing the system to relax and “lose” phase information. Conversely, a faster decay of g means that less time is spent in a region with few fixed points, and therefore the patterns are expected to be more robust.

We first decrease the thresholds of repression of gene A by both genes B and C (Figure 5A). Results of these simulations are shown in Figure 5: Model 2 with a SNIC bifurcation still outperforms Model 1 with Hopf and saddle-node bifurcations. In particular, it is again visually clear on kymographs that Model 2 produces a robust and well-defined pattern at any time point of the simulations, while Model 1 gives rise to a much “fuzzier” pattern before the transition. Model 1 produces a robust static pattern only for a steep gradient (allowing to quickly move through the “fuzzy” phase) and a weak asymmetry in the static module (Figure 5E). It is brittle to any change of the dynamics of g (Figure 5H) or to stronger asymmetry in the static module (Figure 5—figure supplement 1E,H). Conversely, Model 2 is robust to different shapes of the morphogen (Figure 5F,I). Only for a strong asymmetry does the system lose one fixed point (Figure 5—figure supplement 1I), but even in this case transitions through a SNIC bifurcation appear superior to transitions through a Hopf bifurcation.

The fragility of the Hopf bifurcation to asymmetries in the parameters can be understood as follows. In the asymmetric versions of Model 1, one of the fixed points of the static term forms during the Hopf bifurcation, way before the two other fixed points form. It is therefore the only attractor available for a large range of g values. However, in Model 2 the same asymmetry only favors one of the saddle-nodes for a small range of g values,

generating a robust pattern. Again, we can use the mutual information metric defined above to quantify the robustness of the pattern and confirm the superiority of Model 2 (Figure 5—figure supplement 2J). We also confirmed these results for the case of random modifications of the repression thresholds of all interactions in the static term (Figure 5—figure supplement 2).

The asymmetry introduced in Figure 5 changes the shapes of the basins of attraction and the positions of the fixed points. The geometric model allows to change those features independently. The most generic way to introduce an asymmetry in the system is to fix the positions of the fixed points of the static regime and change only the positions of the basins of attraction (the reason is that the future fates depend on the position of the separatrix between different regimes (Corson & Siggia, 2012)). To replicate this situation in the 2D gene-free models, we move the unstable fixed point of the static term along the y axis. Results of this procedure are shown on Figure 6 and confirm our results on the gene-network based models: Model 2 bifurcates via a SNIC and is always more robust than Model 1. When we change the positions of the fixed points in the static regime to move them away from the limit cycle (still in an asymmetric way), interestingly both Models 1 and 2 now bifurcate via SNICs (Figure 6—figure supplement 1). Furthermore, we see that for Model 1, the amplitude of the limit cycle decreases before the bifurcation, while for Model 2, the amplitude increases (Figure 6—figure supplement 1E).

We conclude from all those numerical perturbations that even with asymmetric basins of attraction and asymmetric parameters, transitions based on SNIC bifurcations are both

more generic and more robust than the ones based on Hopf bifurcations, at least in simple low-dimension models.

Spatial wave profiles: Hopf vs SNIC

Our theoretical study suggest that SNIC based transitions are both more robust and more generic than Hopf/saddle-nodes ones. We thus now examine ways to distinguish between Hopf and SNIC based transitions experimentally. The natural method would be to modify the value of the control parameter of the bifurcations (in our case parameter g) and check how the attractors of the system change. A recent experimental example can be found in the auditory hair-bundle context where it has been suggested that Hopf bifurcations can be distinguished from SNIC bifurcations by tuning the external driving force (Salvi, Maoileidigh, & Hudspeth, 2016). However, the situation in development is different from any sensing system since the actual control parameters are not known and are likely combinations of various signaling systems (such as *FGF* or *Wnt*). There could also be many compensatory developmental mechanisms, making it difficult to fully take control of the system, as well known by developmental geneticists.

In the absence of a direct control, we have to rely on indirect measurements. The most obvious choice is to use the antero-posterior position along the embryo (or along the PSM in the case of somite formation) as a proxy for the control parameter. In situs are informative of what locally happens in insects (Ezzat El-Sherif, Averof, & Brown, 2012) (Zhu et al., 2017). In vertebrates, it is possible to monitor in real time segmentation oscillators in embryos (Aulehla et al., 2008) (Webb et al., 2016) (Delaune, François, Shih, & Amacher,

2012) and in tissue cultures (Lauschke, Tsiairis, François, & Aulehla, 2013) (Matsuda et al., 2020) (Diaz-Cuadros et al., 2020), so that many properties of the cycles can be inferred.

A first relevant metric (used in (Salvi et al., 2016)) is the shape of the limit cycle as a function of the control parameter. There is a clear contrast between Hopf and SNIC bifurcations on our simulated kymographs: for Hopf bifurcations, as mentioned above the transition zone is “blurred” because the damped oscillations relax towards the unique fixed point, while for SNIC bifurcations the oscillations localize close to the fixed points, and as a consequence the pattern is gradually reinforced (Figures 2-5; damped oscillations are especially visible in the geometric model). To better visualize the “blurry” transition zone characteristic of Hopf bifurcations in the gene-free model (resp. in the 3-gene model), we compute the distribution of the values of the geometric variables (resp. of the gene concentrations) for different values of parameter g (Figure 7—figure supplement 2). In models with Hopf bifurcations, the distribution becomes very narrow for intermediate values of g, which is a direct consequence of the damped oscillations past the Hopf bifurcations. This suggests that measuring experimentally the distribution of gene concentrations across developmental time at fixed antero-posterior positions can help distinguish SNIC from Hopf bifurcations during actual pattern formation processes. The experimental picture, both from in situs and live imaging, does not support a narrowing of the distribution : it shows clear increases of amplitude that seems more consistent with a gradual reinforcement of the pattern, similar to a SNIC (see e.g. (Delaune et al., 2012)).

Another metric that could help identify the type of bifurcation is the time evolution of the period (resp. of the frequency), which presents a discontinuity for both types of Hopf

bifurcations, but continuously goes to infinity (resp. zero) for SNIC bifurcations. The local spatial wavelength of the pattern provides a continuous measurement related to the local period (as first used and derived in (Francois Giudicelli, Ozbudak, Wright, & Lewis, 2007)). Calling S the somite size (or the wavelength of anterior/posterior markers within somites after clock stopping), $T(x)$ and $S(x)$ the respective period and local wavelength of the pattern at position x (with $x = 0$ being the tail and $x = 1$ the front), and assuming the cells move towards the anterior with constant speed, we have

$$S(x) = \frac{S}{1 - \frac{T(0)}{T(x)}}$$

In the posterior $T(x) = T(0)$, so that $S(x)$ is infinite: all cells are synchronized locally. As cells move towards the anterior, $T(x)$ decays and $S(x)$ decreases but stays bigger than S. If there is a Hopf bifurcation, one expects that the clock will stop with a final period $T(1)$, corresponding to a critical wavelength of the wave $S(1) = S\,\frac{T(1)}{T(1)-T(0)}$, which is strictly greater than S. There is therefore in principle a discontinuity between the wavelength of the propagating wave in the PSM and the wavelength of the static pattern. Conversely, if $T(x)$ goes continuously to infinity, $S(x)$ decays continuously to converge towards S (as measured in (Francois Giudicelli et al., 2007)). This is a simple and intuitive experimental outcome: in this situation the wavelength of the propagating wave in the PSM decreases until it exactly matches the pattern of anterior markers. Therefore, a signature of the finite vs infinite period bifurcation might be visible by comparing the local wavelength of propagating waves in the PSM to the wavelength of anterior markers in the pattern. Practically, monitoring the distance between the peaks of the

oscillations does not give a clear difference between Hopf and SNIC, the reason being that such a discrete measurement can smooth out an abrupt change in the period and that past the Hopf bifurcation, damped oscillations actually give rise to a “ghost” frequency which can decrease quite significantly (see Figure 2—figure supplement 2). Therefore, a measurement of the local wavelength might be less conclusive than a measurement of the amplitude. Nevertheless, we notice that a SNIC scenario gives rise to a combination of an increase of the amplitude with a continuous shrinking of the wavelength, meaning that many refining waves (corresponding to broad variations of periods) will simultaneously propagate.

Finally, SNIC bifurcations are also accompanied by characteristic changes of the shape of spatial wave profiles that might be observable in experiments. We further compare a SNIC-based model to a phase model where an infinite-period behaviour is explicitly assumed, namely the model of a collection of coupled oscillators from (Morelli et al., 2009). A kymograph of the spatio-temporal profile of the frequency imposed on the oscillators is shown in Figure 7A, and the dynamics of the resulting pattern formation process is shown on the kymograph of Figure 7B, with the final pattern on Figure 7C. The most striking difference is observed on the shape of the spatial wave profile as it moves towards the region where the pattern stabilizes. In the infinite-period scenario of (Morelli et al., 2009), the phase profile is by construction symmetric (albeit stretched in the posterior compared to the anterior, see Figure 7E). In the SNIC scenario, we see a clear asymmetry in the peaks of the wave profile (as shown schematically in Figure 7D). Indeed, following the peaks of oscillations spatially from anterior to posterior (left to right), we see that the transition from positive to negative values of y occurs in two steps.

During the first step, the system stays close to $y = 1$ for some time, with y values decreasing slowly, while in the second step the system goes rapidly towards negative y values and reaches $y = -1$ fast (Figure 7F). This phenomenon, which gives rise to a "sawtooth" pattern of propagating waves, is observed in all our versions of Model 2 (and is notably absent from all our versions of Model 1, see Figure 7—figure supplement 1). Those spatial asymmetries are likely due to the asymmetries of the limit cycles of relaxation oscillators, where a system jumps between two (or more) steady states in an asymmetric way (which can also be observed in systems close to criticality, see (Tufcea & François, 2015)). Our model thus offers a simple explanation of wave asymmetry, solving the long-standing problem of the asymmetry of AP vs PA transitions, which is possibly crucial for segment polarity as first suggested by Meinhardt (Meinhardt, 1982).

Discussion

In this work, we have explored the dynamical properties of generic two-module systems, where one module corresponds to a dynamic phase of genetic expression and the other corresponds to a static phase controlling embryonic patterning. The unexpected result is that those models typically present global bifurcations where new fixed points appear on the trajectories in phase space. Such SNIC bifurcations come from the smooth interpolation between a flow defining an oscillator in phase space and a landscape characterized by several fixed points. The oscillating attractor then gets continuously deformed until it breaks into several fixed points, leading to the SNIC. This interpolation is a direct consequence of the assumed two-module control as shown on multiple examples above. Importantly, the overall developmental sequence in this context is emergent, since the dynamics close to the bifurcation cannot be understood independently from the static or dynamic modules only. SNIC bifurcations also provide robustness to various perturbations (since fixed points appearing on cycles better preserve information on the oscillatory phase). Below we detail how this model also recapitulates many observed features of metazoan segmentation.

Experimental Evidence

In absence of a direct handle on the control parameter, comparison of SNIC and Hopf bifurcations in simulated systems reveal three possible signatures of SNIC bifurcations in the propagating antero-posterior waves of genetic expression: 1. oscillations gradually reinforcing the pattern for SNIC (instead of damped oscillations for Hopf) 2.

relaxation-like oscillations leading to some asymmetry in the wave pattern, and 3. a continuous shrinking of the spatial wavelength during the dynamic phase to match the static pattern for SNIC, with many well-defined propagating waves.

For prediction 1, decades of in situs of oscillating genes and of experimental monitoring of *Notch* signalling pathways argue against damped oscillations in somitogenesis. Weak waves gradually refine into well-defined stripes in the anterior PSM, in most species(see for example the comparison made in (Gomez et al., 2008)), suggesting an increase of amplitude in oscillations. Consistent with this, visualising segmentation clock oscillations in live vertebrate embryos suggests an increase of oscillation amplitude as cells get more anterior in the PSM (Delaune et al., 2012; Lauschke et al., 2013). A similar observation was also made for gap genes during short-germ segmentation in *Tribolium* (Zhu et al., 2017).

For prediction 2, in somitogenesis, there is an asymmetry in the wave pattern before stabilization. The transition from the high to low phase within one somite is shallower than the transition between those two phases from one somite to the other (i.e. posterior of one somite to anterior of the next), as detailed in (Shih et al., 2015). A possible read-out is the downstream pattern of *Cadherin* controlling segment boundary formation, which presents a sawtooth profile (McMillen, Chatti, Julich, & Holley, 2016), consistent with the observed asymmetry in the wave pattern. It has been proposed that the main reason for the clock control was precisely to generate such periodic sawtooth pattern, and a SNIC bifurcation offers a plausible mechanism. In insects, it has been proposed that one of the roles of traveling waves of segmentation genes (e.g. *eve* genes shift) is indeed to provide segment polarity (Rothschild, Tsimiklis, Siggia, & François, 2016) (Clark,

2017; Clark & Akam, 2016), which is consistent with this proposal, although precise quantification of wave asymmetry has not been done in this context to our knowledge. In situs of gap genes in short germ insects show asymmetry between the anterior and posterior borders of the propagating gene expression waves as well (Zhu et al., 2017).

For prediction 3, the slowdown of oscillations during vertebrate segmentation appears quite variable between species. Mouse segmentation clock seems at first more consistent with a relatively sudden Hopf scenario. There is roughly a 2π phase shift between the posterior and the front, consistent with only a moderate change of the period/wavelength (Lauschke et al., 2013). Other species have several propagating waves within the PSM, seemingly more consistent with a broader period regime. In zebrafish, in vivo real-time imaging suggests a wavelength of propagating waves in the anterior PSM of roughly twice the segment length, meaning that the period of the clock at the front is at least half of the period in the tail bud (Shih, François, Delaune, & Amacher, 2015). However, this measurement likely overestimates the wavelength and thus underestimates the period at the front since it is based on a peak to peak measurement between the last two waves. Thus the period of the clock might further increase in the anterior, consistent with a period divergence and with measurements of (Francois Giudicelli et al., 2007) on in situs, who proposed that the period indeed diverges (Francois Giudicelli et al., 2007). Importantly, as said above, while the period increases the amplitude increases too (Shih et al., 2015), which is more consistent with a SNIC bifurcation. In situs in snake PSM clearly show a decrease of the wavelength that seems to continuously match the pattern in the anterior, possibly more consistent with an infinite-period bifurcation as well (Gomez et al., 2008).

A direct experimental measure of the wavelength of the pattern for the last oscillations can be found with *Mesp2* (Koseki et al., 2000) (Saga & Takeda, 2001). The consensus on *Mesp2* is that it is expressed in the last few waves of oscillations, and that its pattern continuously regresses to reach exactly the wavelength of the anterior pattern. This is consistent with an infinite-period bifurcation. In (Oginuma et al., 2010) it is argued that Mesp helps setting the segment boundary in mouse by precisely reading the Notch wave, explaining both its biological role and why it is a convenient marker of the wavelength. We notice that the model used to explain the experiments in (Oginuma et al., 2010) is Julian Lewis' model from the appendix of (Palmeirim et al., 1997), thus presenting an infinite-period divergence.

One cannot completely exclude from all those experimental observations a Hopf scenario where waves would not be very damped (or would be amplified for some reason) past the bifurcation, while the period of damped oscillations would become long until the saddle-node bifurcation is reached. A way to experimentally falsify this scenario is to induce a smoother transition and see if damped oscillations appear. Interestingly, both in vertebrates and in short germ insects, changes of *Wnt* signalling indeed give rise to smoother transitions from the dynamic to the static regime (suggesting that *Wnt* could be related to the control parameter g). In mouse, *beta-catenin* gain of function mutants give rise to considerably extended PSM towards the anterior (Aulehla et al., 2008), with up to 5 waves of oscillating *Lfng* (compared to only one in WT). Thus, this extended PSM qualitatively looks much more like a zebrafish or a snake PSM, with reinforcement of *Lfng* in situs from anterior to posterior (suggesting a refinement of the pattern and not damped oscillations, see (Aulehla et al., 2008, see Figure 4g,h)). In the anterior PSM of

such mutants, the wavelength of the oscillations decreases to match exactly the *Mesp2* wavelength (Aulehla et al., 2008, see e.g. Fig 3), and the very last waves move extremely slowly towards the anterior (Alexander Aulehla, private communication), consistent with a divergence of the time-scale. In *Tribolium*, *axin* RNAi similarly changes the wave pattern, where smoother and more spatially extended propagation of gap gene expressions are observed in those mutants, with reduced wavelengths compared to the WT (see Fig. 4 of (Zhu et al., 2017)). Those phenotypes are exactly what is expected from an infinite-period bifurcation, again consistent with the SNIC scenario.

Lastly, damped oscillations would also be absent from Hopf scenarios where the bifurcation that destroys the limit cycle occurs at a value of the control parameter that is almost exactly the value at which the system becomes multistable. This happens for example when the supercritical Hopf bifurcation that kills the limit cycle happens at the same value of parameter g than the pitchfork bifurcation that generates bistability (Figure 4—figure supplement 1F). A similar phenomenon occurs in the model presented on Figure 4—figure supplement 4: the two simultaneous subcritical Hopf bifurcations that generate the bistability and the saddle-node of limit cycles that destroys the stable limit cycle happen in a very narrow range of g values. We cannot fully exclude those cases from the experimental data, but we notice they are intrinsically less generic since multiple bifurcations have to occur at the same time, which happens only in our models because of specific parameter choices, symmetries in the equations or specific choices of non-linearity for the weights of the modules.

Model Predictions

The most straightforward prediction of the model proposed here is the presence of several global transcriptional modules between strongly interacting genes, directly controlling the smooth changes of developmental time-scale (in a similar way to the "speed-gradient" model in (Zhu et al., 2017)). Many developmental genes are regulated by multiple "shadow" enhancers (Cannavò et al., 2016). A smooth transition between different enhancers has even been observed for gap genes in *Drosophila* (El-Sherif & Levine, 2016). Global regulation of transcriptional modules could be biologically achieved through "super enhancers" regulating many genes at the same time (Hnisz et al., 2017). A non-trivial prediction of our model is that the intrinsic time-scale of the system is a function of the relative balance of transcriptional activities of the modules. The transcriptional control described here naturally allows for infinite-period bifurcations, an implicit mechanism in several models of metazoan segmentation. This is to be contrasted with classical models of negative feedback oscillators such as the Goodwin model, where the time-scale is entirely controlled by degradation and is independent from transcription and translation rates (Forger, 2011), and with models of delayed oscillators, where the time-scale is essentially controlled by transcriptional delays (Lewis, 2003).

Our model is controlled by an external parameter g. The most natural hypothesis would be that g corresponds to an actual morphogen gradient. As said above, *Wnt* is a natural candidate, but feedbacks clearly exist with *Caudal* in *Tribolium* (Zhu et al., 2017) and *FGF* in vertebrates. However, in the spirit of the initial wavefront proposal by Cooke and Zeeman, g could also be in some context a temporal variable, e.g. an effective timer.

Recent works on somitogenesis have suggested that the segmentation front could also be coupled to the slowing down of two oscillators (Lauschke et al., 2013), possibly one corresponding to *Notch/FGF* and the other to *Wnt* (Sonnen et al, 2018), so that the oscillation could feedback on itself to define g. One could also imagine that g is related to more biophysical variables (density, elasticity) (Hubaud, Regev, Mahadevan, & Pourquie, 2017). It is important to point out that in our framework the nature of the bifurcation does *not* depend on the nature of g. While it might be difficult to experimentally disentangle feedbacks between the bifurcations and the control parameter from actual properties of the bifurcations themselves, our predictions on the nature of the bifurcations would not change.

An assumption of this two-module framework is that the same genes interact to control the system in *both* the dynamic and static regimes, giving rise to a smooth dynamical transition during development. This is consistent with what is observed for gap gene dynamics in short germ insects (Zhu et al., 2017). For vertebrate segmentation, we do not know yet mechanistically how both regimes are controlled, but the *Notch* signalling pathway is implicated in all steps of somitogenesis and in particular is known to gate information from the oscillatory to the segmented regime (Oginuma et al., 2010). An opposite view would be that the transition from dynamic to static regime is *de facto* sudden (even if it appears smooth for other reasons). Such scenario could be realized in different ways. For instance, different enhancers could regulate completely different sets of genes in the dynamic vs static regimes. The “static” genes would then interact with the “dynamic” genes only briefly during development, ensuring transmission of positional information between the static and dynamic regimes in a very localized region

of time and space. In somitogenesis, as said above specific genes are indeed expressed at the so-called “front” (such as *Mesp2*) and could act like gating processes transferring the information from the clock to an independent patterning system. In this case, we would be back to a sequential point of view where different regimes of development live in different regions of phase space, and the local bifurcation scenario would then be more plausible.

Evolution and developmental plasticity

Evolutionary simulations for the evolution of patterning have favored a scenario based on Hopf and saddle-node bifurcations (François et al., 2007). Those simulations did not include multiple enhancers like here, and all transcriptional regulations had essentially to evolve from scratch, possibly suggesting a “Ur-segmentation clock” based on Hopf and saddle-node bifurcations. This scenario is not excluded by our model: in particular there would be no difference between Hopf and SNIC bifurcations under the control of steep gradients of g, which shortcut the region where only one fixed point is present. So Hopf/saddle node bifurcations under control of a steep gradient are likely the easiest solution found by (simulated) evollution. However, adding a more complex, enhancer-based evolutionary grammar might allow for more combinatorial use of dynamical attractors, and associated robustness to external perturbations (such as the shape of the g gradient). A SNIC bifurcation might then plausibly evolve from the modularization (West-Eberhard, 2003) of a system based on Hopf and saddle-node bifurcations (both *in vivo* and *in silico*). First, since the SNIC bifurcation is the generic scenario that we observe in our framework, it should be easy to discover by evolution once a multi-

enhancer system combining an oscillator and a bistable system has evolved. Second, SNIC-controlled segmentation is plastic in the sense that changes of dynamics of the control parameter would change the transient phenotypes (such as the number of oscillating waves) but would still generate a pattern. Modularizations leading to developmental plasticity has been suggested to be an important engine for evo-devo (West-Eberhard, 2003), since it allows for intra-specific variability without impinging on the most important phenotypes (here, segmentation).

Importantly, such plasticity is indeed observed experimentally both for short germ and vertebrate segmentation. For instance, in *Tribolium* one can considerably modify *Caudal* gradient dynamics and still see proper patterning (Zhu et al., 2017). It could thus explain how and why there is so much quantitative variability in segmentation mechanisms, such as short vs intermediate germ band segmentation (as suggested in (Zhu et al., 2017)), In somitogenesis, there is a lot of interspecies quantitative variability in the numbers of waves and rescaled periods (Gomez et al., 2008)) while the qualitative dynamics itself appears very conserved see e.g. (Krol et al., 2011) . In other words, a two-module mechanism makes the dynamics both more robust – a generic bifurcation scenario gives precise phase encoding – and more evolvable – one can vary many features of the system (e.g. basins of attractions, dynamics of the control parameter) and still get proper patterning, again a hallmark of developmental plasticity.

In brief, we have discussed a two-module based model of the smooth transition in development from a dynamical regime to a static one. This model explains time-scale divergence, as well as robustness to changes of morphogen dynamics (Zhu et al., 2017)

and to noise. It provides a possible explanation for smooth robust transitions in metazoan segmentation, with a non-trivial (global) bifurcation. Further experimental and theoretical studies are required to assess the importance of smooth transitions for encoding dynamic information into spatial patterns of genetic expressions.

Acknowledgements

We thank members of the François and El-Sherif groups for insightful discussions, as well as referees for their insightful comments.

This work was supported by a CREATE : Complex Dynamics fellowship to L. Jutras-Dubé, a DFG grant EL 870/2-1 to E. El-Sherif, a NSERC Discovery Grant and a Simons Investigator in Mathematical Modelling of Living Systems to P. François.

Competing Interests

The authors declare that no competing interests exist.

References

Ares, S., Morelli, L. G., Jörg, D. J., Oates, A. C., & Jülicher, F. F. (2012). Collective modes of coupled phase oscillators with delayed coupling. *Physical Review Letters*, *108*(20), 204101.

Aulehla, A., Wiegraebe, W., Baubet, V., Wahl, M. B., Deng, C., Taketo, M., . . . Pourquié, O. (2008). A beta-catenin gradient links the clock and wavefront systems in mouse embryo segmentation. *Nat Cell Biol, 10*(2), 186-193.

Beaupeux, M., & François, P. (2016). Positional information from oscillatory phase shifts : insights from in silico evolution. *Physical Biology*, *13*(3), 1–14.

Cannavò, E., Khoueiry, P., Garfield, D. A., Geeleher, P., Zichner, T., Gustafson, E. H., Ciglar, L., Korbel, J. O., & Furlong, E. E. M. (2016). Shadow enhancers are pervasive features of developmental regulatory networks. *Current Biology*, *26*(1), 38–51.

Clark, E. (2017). Dynamic patterning by the Drosophila pair-rule network reconciles long-germ and short-germ segmentation. *PLoS Biol, 15*(9), e2002439.

Clark, E., & Akam, M. (2016). Odd-paired controls frequency doubling in Drosophila segmentation by altering the pair-rule gene regulatory network. *eLife, 5*.

Cooke, J., & Zeeman, E. C. (1976). A clock and wavefront model for control of the number of repeated structures during animal morphogenesis. *Journal of Theoretical Biology*, *58*(2), 455–476.

Corson, F., Couturier, L., Rouault, H., Mazouni, K., & Schweisguth, F. (2017). Self-organized Notch dynamics generate stereotyped sensory organ patterns in Drosophila. *Science*, *356*(6337), eaai7407.

Corson, F., & Siggia, E. D. (2012). Geometry, epistasis, and developmental patterning. *Proceedings of the National Academy of Sciences*, *109*(15), 5568–5575.

Corson, F., & Siggia, E. D. (2017). Gene free methodology for cell fate dynamics during development. *ELife*, *6*, e30743.

Dale, J. K., Maroto, M., Dequeant, M. L., Malapert, P., McGrew, M., & Pourquie, O. (2003). Periodic notch inhibition by lunatic fringe underlies the chick segmentation clock. *Nature, 421*(6920), 275-278.

Delaune, E. A., François, P., Shih, N. P., & Amacher, S. L. (2012). Single-Cell-Resolution Imaging of the Impact of Notch Signaling and Mitosis on Segmentation

Clock Dynamics. *Developmental Cell, 23*(5), 995-1005

Dequeant, M.-L., Glynn, E., Gaudenz, K., Wahl, M., Chen, J., Mushegian, A., & Pourquié, O. (2006). A complex oscillating network of signaling genes underlies the mouse segmentation clock. *Science, 314*(5805), 1595-1598.

Diaz-Cuadros, M., Wagner, D. E., Budjan, C., Hubaud, A., Tarazona, O. A., Donelly, S., . . . Pourquie, O. (2020). In vitro characterization of the human segmentation clock. *Nature, 580*(7801), 113-118.

Dubrulle, J., & Pourquié, O. (2004). fgf8 mRNA decay establishes a gradient that couples axial elongation to patterning in the vertebrate embryo. *Nature*, 419–422.

El-Sherif, E., Averof, M., & Brown, S. J. (2012). A segmentation clock operating in blastoderm and germband stages of Tribolium development. *Development*, *139*(23), 4341–4346.

El-Sherif, E., & Levine, M. (2016). Shadow enhancers mediate dynamic shifts of gap gene expression in the drosophila embryo. *Current Biology*, *26*(9), 1164–1169.

Elowitz, M. B., & Leibler, S. (2000). A synthetic oscillatory network of transcriptional regulators. *Nature*, *403*(6767), 335–338.

Ermentrout, B. (2008). Ermentrout-Kopell canonical model. *Scholarpedia, 3*(3), 1398.

Forger, D. B. (2011). Signal processing in cellular clocks. *Proceedings of the National Academy of Sciences*, *108*(11), 4281–4285.

François, P., Hakim, V., & Siggia, E. D. (2007). Deriving structure from evolution: metazoan segmentation. *Molecular Systems Biology*, *3*, 9.

François, P., & Siggia, E. D. (2012). Phenotypic models of evolution and development: geometry as destiny. *Current Opinion in Genetics & Development*, *22*(6), 627–633.

Gillespie, D. T. (2001). Approximate accelerated stochastic simulation of chemically reacting systems. *The Journal of Chemical Physics*, *115*(4), 1716.

Giudicelli, François, & Lewis, J. (2004). The vertebrate segmentation clock. *Current Opinion in Genetics & Development*, *14*(4), 407–414.

Giudicelli, F., Ozbudak, E. M., Wright, G. J., & Lewis, J. (2007). Setting the tempo in development: an investigation of the zebrafish somite clock mechanism. *PLoS Biology*, *5*(6), e150.

Gomez, C., Ozbudak, E. M., Wunderlich, J., Baumann, D., Lewis, J., & Pourquié, O. (2008). Control of segment number in vertebrate embryos. *Nature*, *454*(7202), 335–339.

Graf, T., & Enver, T. (2009). Forcing cells to change lineages. *Nature*, *462*(7273), 587–594.

Hnisz, D., Shrinivas, K., Young, R. A., Chakraborty, A. K., & Sharp, P. A. (2017). A phase separation model for transcriptional control. *Cell, 169*(1), 13–23.

Huang, S., Guo, Y., May, G., & Enver, T. (2007). Bifurcation dynamics in lineage-commitment in bipotent progenitor cells. *Developmental Biology*, *305*(2), 695–713.

Hubaud, A., Regev, I., Mahadevan, L., & Pourquie, O. (2017). Excitable Dynamics and Yap-Dependent Mechanical Cues Drive the Segmentation Clock. *Cell, 171*(3), 668-682 e611.

Jaeger, J., & Monk, N. (2014). Bioattractors: dynamical systems theory and the evolution of regulatory processes. *The Journal of Physiology*, *592*(11), 2267–2281.

Jiang, Y. J., Aerne, B. L., Smithers, L., Haddon, C., Ish-Horowicz, D., & Lewis, J. (2000). Notch signalling and the synchronization of the somite segmentation clock. *Nature*,

408(6811), 475–479.

Jörg, D. J., Morelli, L. G., Soroldoni, D., Oates, A. C., & Jülicher, F. (2015). Continuum theory of gene expression waves during vertebrate segmentation. *New Journal of Physics, 17*(9), 093042.

Koseki, H., Saga, Y., Takahashi, Y., Koizumi, K., Takagi, A., Kitajima, S., & Inoue, T. (2000). Mesp2 initiates somite segmentation through the Notch signalling pathway. *Nature Genetics*, *25*(4), 390–396.

Krol, A. J., Roellig, D., Dequéant, M.-L., Tassy, O., Glynn, E., Hattem, G., Mushegian, A., Oates, A. C., & Pourquié, O. (2011). Evolutionary plasticity of segmentation clock networks. *Development*, *138*(13), 2783–2792.

Lauschke, V. M., Tsiairis, C. D., François, P., & Aulehla, A. (2013). Scaling of embryonic patterning based on phase-gradient encoding. *Nature*, *493*(7430), 101–105.

Lewis, J. (2003). Autoinhibition with transcriptional delay: a simple mechanism for the zebrafish somitogenesis oscillator. *Current Biology*, *13*(16), 1398–1408.

Matsuda, M., Yamanaka, Y., Uemura, M., Osawa, M., Saito, M. K., Nagahashi, A., . . . Alev, C. (2020). Recapitulating the human segmentation clock with pluripotent stem cells. *Nature, 580*(7801), 124-129.

McMillen, P., Chatti, V., Julich, D., & Holley, S. A. (2016). A Sawtooth Pattern of Cadherin 2 Stability Mechanically Regulates Somite Morphogenesis. *Curr Biol, 26*(4), 542-549.

Meinhardt, H. (1982). *Models of biological pattern formation*. New York, NY: Academic Press.

Meinhardt, H. (1986). Models of segmentation. In *Somites in developing embryos* (pp. 179–189). Boston, MA: Springer.

Morelli, L. G., Ares, S., Herrgen, L., Schröter, C., Jülicher, F. F., & Oates, A. C. (2009).

Delayed coupling theory of vertebrate segmentation. *HFSP Journal*, *3*(1), 55–66.

Morelli, L. G., & Jülicher, F. F. (2007). Precision of genetic oscillators and clocks. *Physical Review Letters*, *98*(22), 228101.

Murray, P. J., Maini, P. K., & Baker, R. E. (2013). Modelling Delta-Notch perturbations during zebrafish somitogenesis. *Developmental Biology*, *373*(2), 407–421.

Oginuma, M., Takahashi, Y., Kitajima, S., Kiso, M., Kanno, J., Kimura, A., & Saga, Y. (2010). The oscillation of Notch activation, but not its boundary, is required for somite border formation and rostral-caudal patterning within a somite. *Development*, *137*(9), 1515–1522.

Palmeirim, I., Henrique, D., Ish-Horowicz, D., & Pourquié, O. (1997). Avian hairy gene expression identifies a molecular clock linked to vertebrate segmentation and somitogenesis. *Cell*, *91*(5), 639–648.

Poston, T., & Stewart, I. (2012). *Catastrophe theory and its applications*. London: Dover Publications.

Pusuluri, S. T., Lang, A. H., Mehta, P., & Castillo, H. E. (2018). Cellular reprogramming dynamics follow a simple 1D reaction coordinate. *Physical Biology*, *15*(1), 16001.

Rothschild, J. B., Tsimiklis, P., Siggia, E. D., & François, P. (2016). Predicting Ancestral Segmentation Phenotypes from Drosophila to Anopheles Using In Silico Evolution. *PLoS Genetics, 12*(5), e1006052-1006019.

Rudolf, H., Zellner, C., & El-Sherif, E. (2020). Speeding up anterior-posterior patterning of insects by differential initialization of the gap gene cascade. *Dev Biol, 460*(1), 20-31.

Saga, Y., & Takeda, H. (2001). The making of the somite: molecular events in vertebrate segmentation. *Nat Rev Genet, 2*(11), 835-845.

Salvi, J. D., Maoileidigh D. O., & Hudspeth, A. J. (2016). Identification of Bifurcations from Observations of Noisy Biological Oscillators. *Biophys J, 111*(4), 798-812.

Sarrazin, A. F., Peel, A. D., & Averof, M. (2012). A segmentation clock with two-segment periodicity in insects. *Science*, *336*(6079), 338–341.

Schwendinger-Schreck, J., Kang, Y., & Holley, S. A. (2014). Modeling the Zebrafish Segmentation Clock's Gene Regulatory Network Constrained by Expression Data Suggests Evolutionary Transitions Between Oscillating and Nonoscillating Transcription. *Genetics, 197*(2), 725-738.

Shih, N. P., François, P., Delaune, E. A., & Amacher, S. L. (2015). Dynamics of the slowing segmentation clock reveal alternating two-segment periodicity. *Development*, *142*(10), 1785–1793.

Sonnen, K. F., Lauschke, V. M., Uraji, J., Falk, H. J., Petersen, Y., Funk, M. C., Beaupeux, M., François, P., Merten, C. A., & Aulehla, A. (2018). Modulation of phase shift between Wnt and Notch signaling oscillations controls mesoderm segmentation. *Cell*, *172*(5), 1079–1090.e12.

Strogatz, S. H. (2015). *Nonlinear dynamics and chaos: with applications to physics, biology, chemistry, and engineering*. Boca Raton, FL: CRC Press.

Tufcea, D. E., & François, P. (2015). Critical Timing without a Timer for Embryonic Development. *Biophysj, 109*(8), 1724-1734.

Verd, B., Clark, E., Wotton, K. R., Janssens, H., Jiménez-Guri, E., Crombach, A., & Jaeger, J. (2018). A damped oscillator imposes temporal order on posterior gap

gene expression in Drosophila. *PLoS Biology*, *16*(2), e2003174.

Waddington, C. H. (1957). *The strategy of the genes*. London: Routledge.

West-Eberhard, M-J (2003). *Developmental Plasticity and Evolution .* Oxford University Press

Webb, A. B., Lengyel, I. M., Jörg, D. J., Valentin, G., Jülicher, F. F., Morelli, L. G., . . . Whitfield, T. T. (2016). Persistence, period and precision of autonomous cellular oscillators from the zebrafish segmentation clock. *eLife, 5*, e08438.

Wolpert, L., Smith, J., Jessel, T., Lawrence, P., Robertson, E., & Meyerowitz, E. (2006). *Principles of development*. Oxford University Press.

Wright, G. J., Giudicelli, F., Soza-Ried, C., Hanisch, A., Ariza-McNaughton, L., & Lewis, J. (2011). DeltaC and DeltaD interact as Notch ligands in the zebrafish segmentation clock. *Development, 138*(14), 2947-2956.

Zhu, X., Rudolf, H., Healey, L., François, P., Brown, S. J., Klingler, M., & El-Sherif, E. (2017). Speed regulation of genetic cascades allows for evolvability in the body plan specification of insects. *Proceedings of the National Academy of Sciences*, *114*(41), E8646–E8655.

Figures

High resolution versions of all figures can be found at https://github.com/laurentjutrasdube/Dual-Regime_Geometry_for_Embryonic_Patterning/tree/master/Figures

Figure 1: Scenarios for segment formation. (*A*) General phenomenology of

segment or somite formation. The white to blue gradient represents the oscillating system (e.g. some Notch signaling pathway gene). The determination front (red vertical line) sweeps the embryo in the posterior direction (red arrow) and translates the periodic expression of a genetic clock into a spatial pattern. (*B-F*) Pattern formation with the infinite-period scenario. (*B*) Period divergence is imposed as control parameter g decreases from 1 to 0. (*C*) Two simulated cells with the same dynamics of g end up with different final values of the phase. (*D-E*) Kymographs showing respectively the dynamics of parameter g used in the simulated embryo and the dynamics of the genetic clock. (*F*) Schematic of the final pattern. (*G-K*) Pattern formation with the Hopf scenario. (*G*) Schematic of the gene regulatory network. (*H*) Depending on the dynamics of g, simulated cells can end up with either a high or a low concentration of protein *E*. (*I-J*) Kymograph showing respectively the dynamics of parameter *g* used in the simulated embryo and the dynamics of protein *E*. (*K*) Schematic of the final pattern. The boundary between two segments ("S_i") is set arbitrarily at the transition from high to low concentrations of protein *E*.

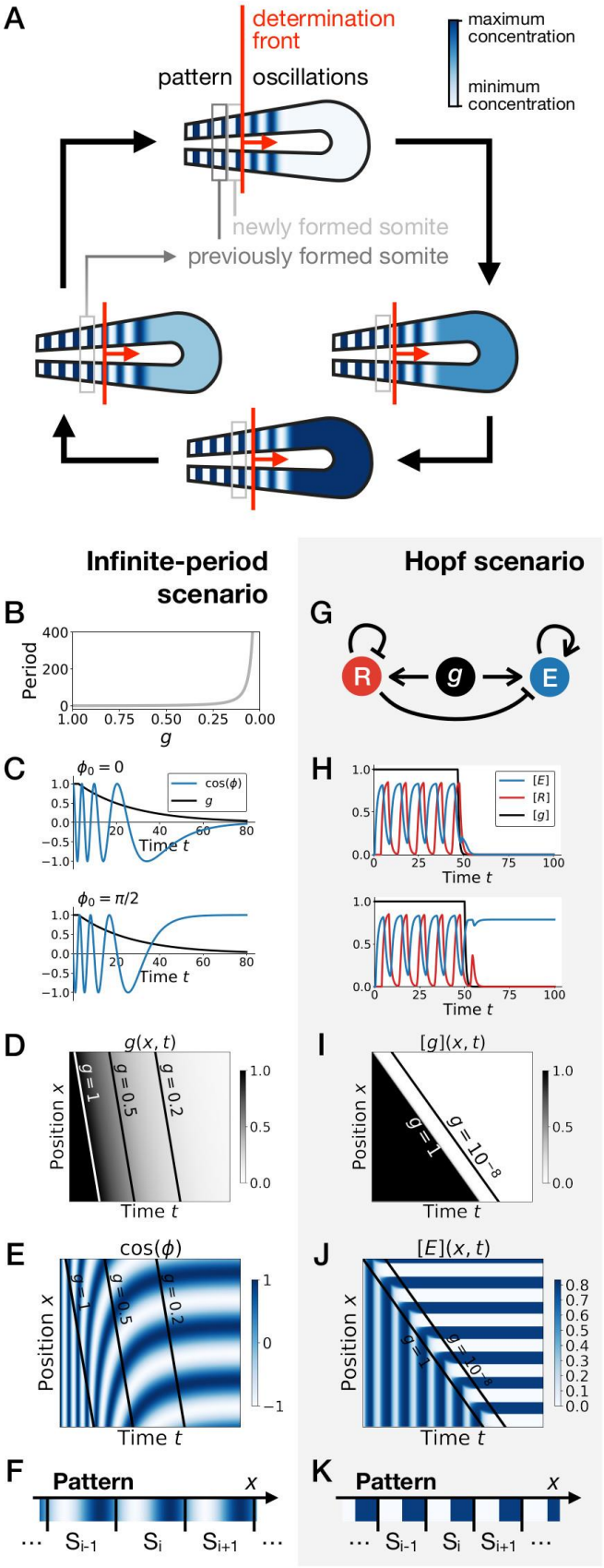

Figure 2: 3-gene models for pattern formation. (*A*) Schematic of the gene regulatory networks encoded by the dynamic term (dotted line) and the static term (solid line). (*B*) Kymograph showing the dynamics of parameter g used in the simulated embryos for both Models 1 and 2. (*C-H*) Simulation results for Model 1. (*C*) Weights of the dynamic (dotted line) and static (solid line) modules as a function of parameter g. (*D*) Gene concentration and value of parameter g inside a representative simulated cell as a function of time. (*E*) Kymograph showing the dynamics of gene expression in the simulated embryo. Transparent colors are used to represent the concentration of the 3 genes, so that mixes of the 3 genes can be easily perceived. Genes *A*, *B*, and *C* are shown in transparent white, blue and purple, respectively. Simulated cells with intermediate concentrations of all genes appear grey. (*F*) Schematic of the final pattern. (*G*) Bifurcation diagram showing the types of dynamics available to the simulated embryo as a function of parameter g. The maximum and minimum concentrations of gene *A* on the stable limit cycles are shown in black. Stable and unstable fixed points are shown in green and red, respectively. "SN" stands for

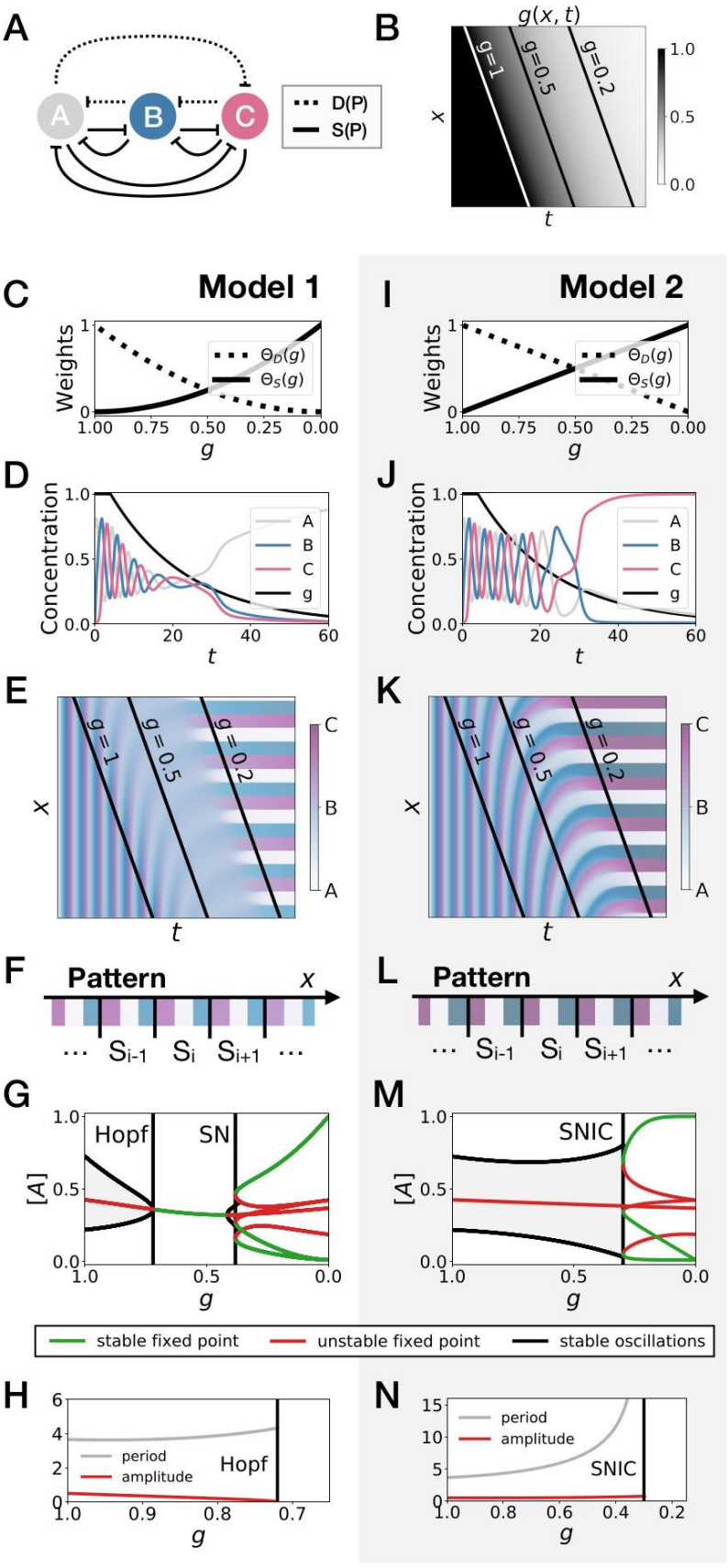

saddle-node bifurcation. (*H*) Period (grey line) and amplitude (red line) of the oscillations along the stable limit cycle. (*I*-*N*) Simulation results for Model 2.

Figure 3: Stochastic simulations of the 3-gene models. (*A-D*) Kymographs showing the stochastic dynamics of gene expression in simulated embryos. The specific values of the typical concentration Ω and of the diffusion constant *D* used to generate each kymograph are indicated on the panels. The concentration of the three genes at the last simulated time point is shown schematically in the lower part of each panel. (*E*) Mutual information as a function of typical concentration Ω for Model 1 (red lines) and Model 2 (black lines). Paler colors correspond to lower values of the diffusion constant *D.* The thick horizontal black line indicates the ideal mutual information for 3 mutually exclusive genes. Note that higher values of Ω correspond to lower noise levels.

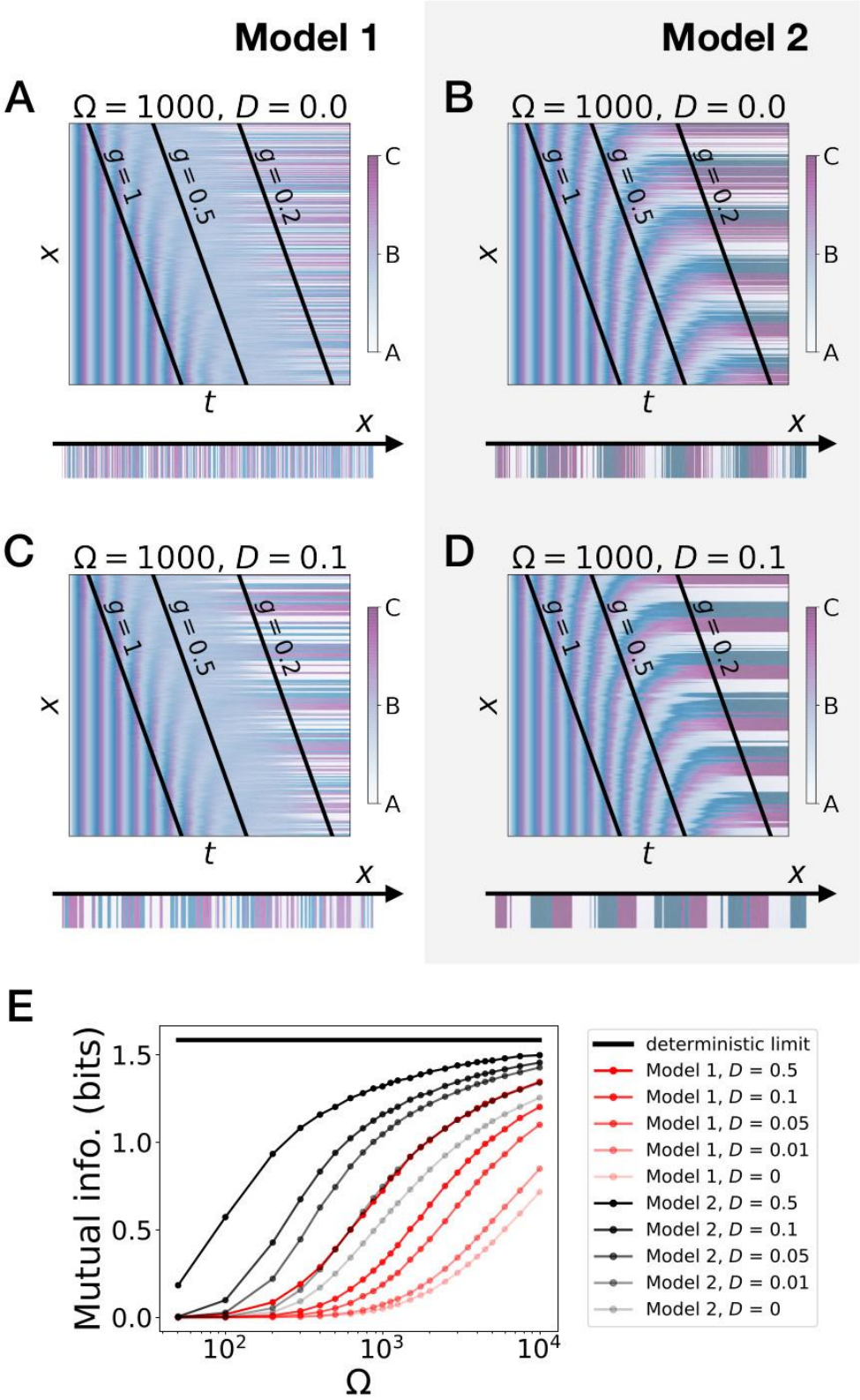

Figure 4: Gene-free geometric model for pattern formation (Model 2). (*A*) Schematic of the flow encoded by the dynamic and static terms. The grey circle represents oscillations on the unit circle. Green and red dots represent unstable and stable fixed points, respectively. (*B*) Weights of the dynamic (dotted line) and static (solid line) modules as a function of parameter g. (*C*) Values of geometric coordinates y and z and of parameter g in a simulated cell as a function of time. (*D-E*) Kymographs showing respectively the dynamics of parameter g used in the simulated embryo and the dynamics of coordinate y. (*F*) Schematic of the final pattern. (*G*) Bifurcation diagram showing the types of dynamics available to the simulated embryo as a function of parameter g. The maximum and minimum values of coordinate y on the stable limit cycles are shown in black. Stable and unstable fixed points are shown in green and red, respectively. (*H*) Period and amplitude of the oscillations. (*I*) Flow in phase space for different values of parameter g. The same color scheme than panel *A* is used to represent the cycles and the fixed points. Positions along the limit cycle at time points separated by a fixed time interval are indicated with black dots, so that variations of the speed of the oscillations along the limit cycle can be visualized. The yellow and orange lines represent the y and z

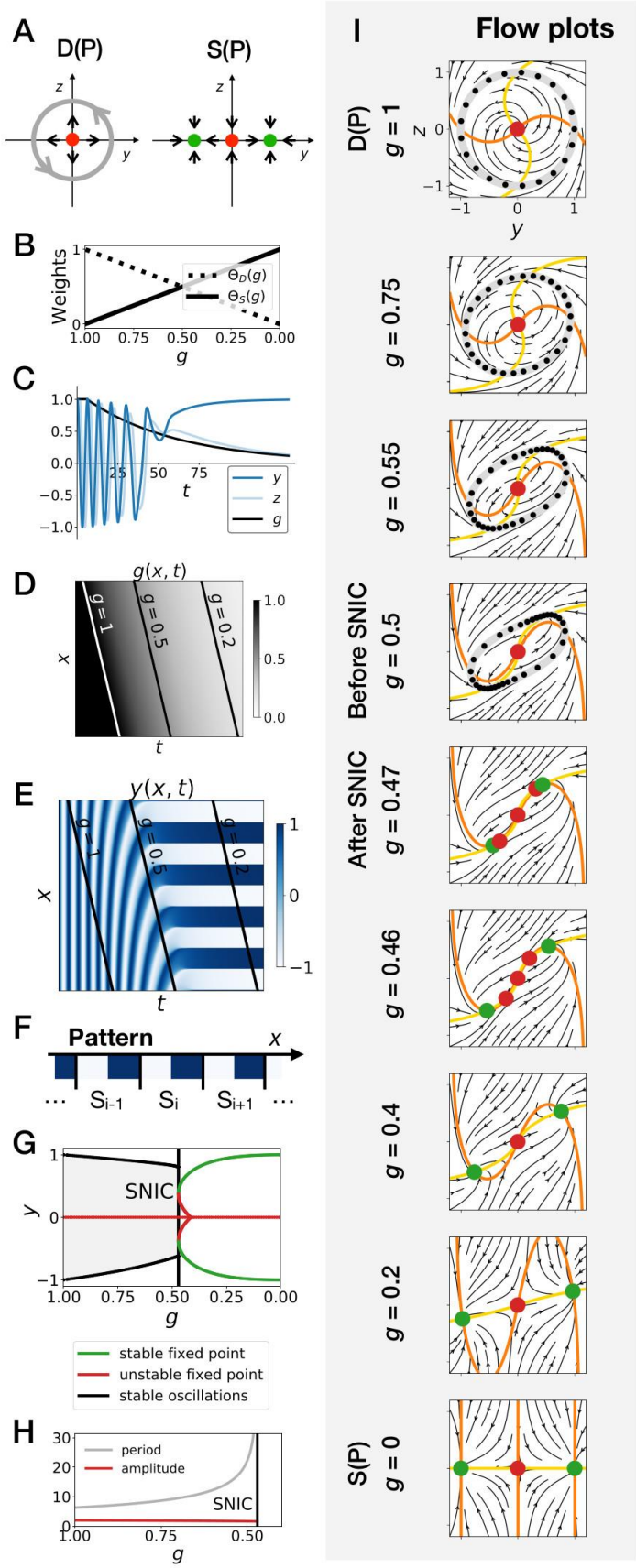

nullclines, respectively.

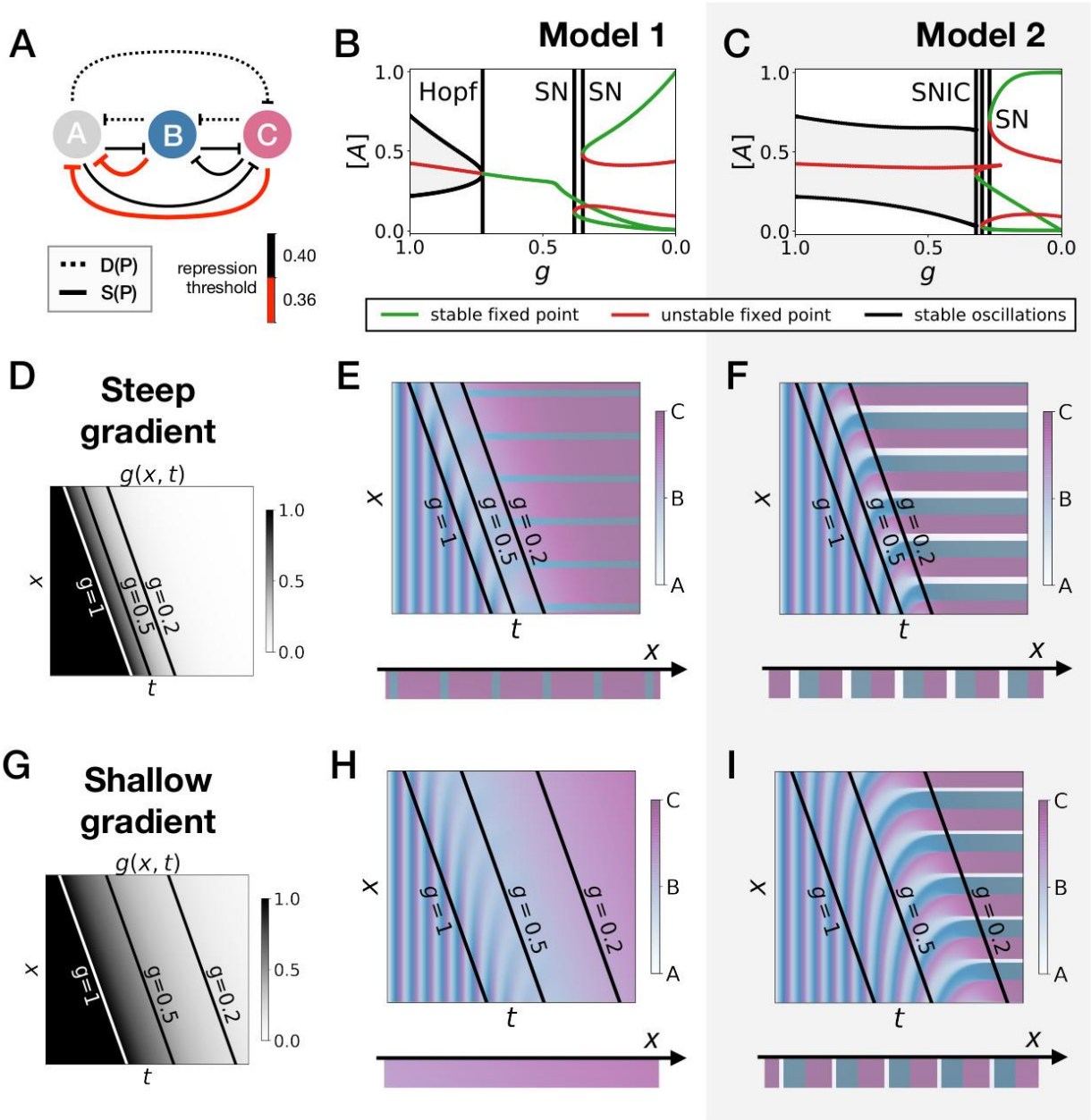

Figure 5: Perturbation of the morphogen gradient steepness in asymmetric 3-gene models. (*A*) Schematic of the gene regulatory networks encoded by the dynamic term (dotted line) and the static term (solid line). The thick red lines indicate stronger repression than the black lines (see the parameters in the Appendix). (*B-C*) Bifurcation diagram showing the types of dynamics available in Models 1 and 2. The maximum and minimum concentrations of gene *A* on the stable limit cycles are shown in black. Stable and unstable fixed points are shown in green and red, respectively. The main bifurcations are identified with vertical lines. "SN" stands for saddle-node bifurcation. (*D-F*) Simulation

results for a steep gradient of parameter g. (*D*) Kymograph showing the dynamics of parameter g used in the simulated embryos for both Models 1 and 2. (*E-F*) Kymograph showing the dynamics of gene expression in the simulated embryo of Models 1 and 2. The concentration of the three genes at the last simulated time point is shown schematically in the lower part of the panels. (*H-J*) Simulation results for a shallow gradient of parameter g.

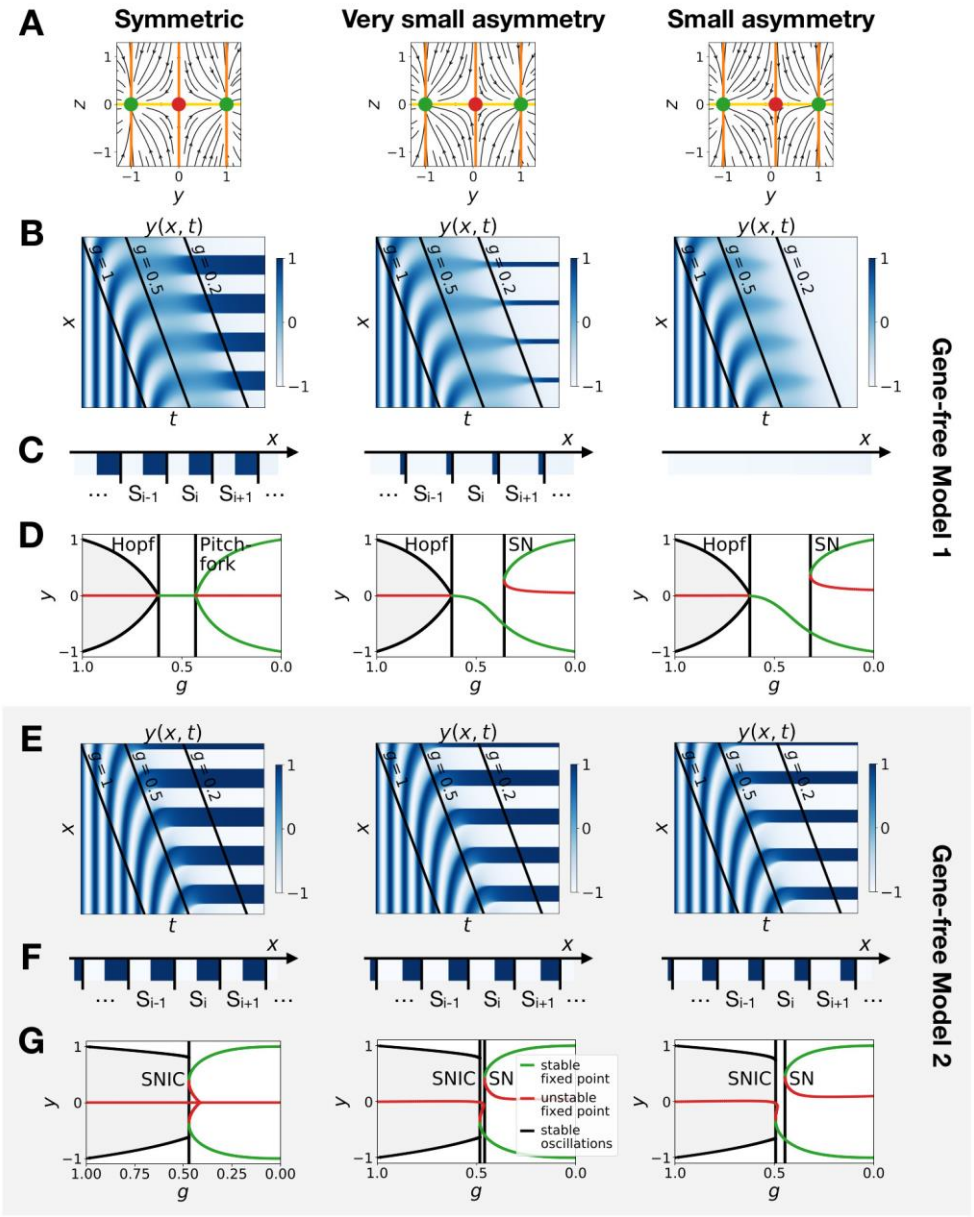

Figure 6: Perturbation of the morphogen gradient steepness in the gene-free geometric models. (*A*) Flow plots showing the changes of geometry of the static module. (*B-C*) Corresponding kymographs and final patterns for Model 1. (*D*) Associated bifurcations diagrams. "SN" stands for saddle-node bifurcation. (*E-F*) Corresponding kymographs and final patterns for Model 2. (*G*) Associated bifurcation diagrams.

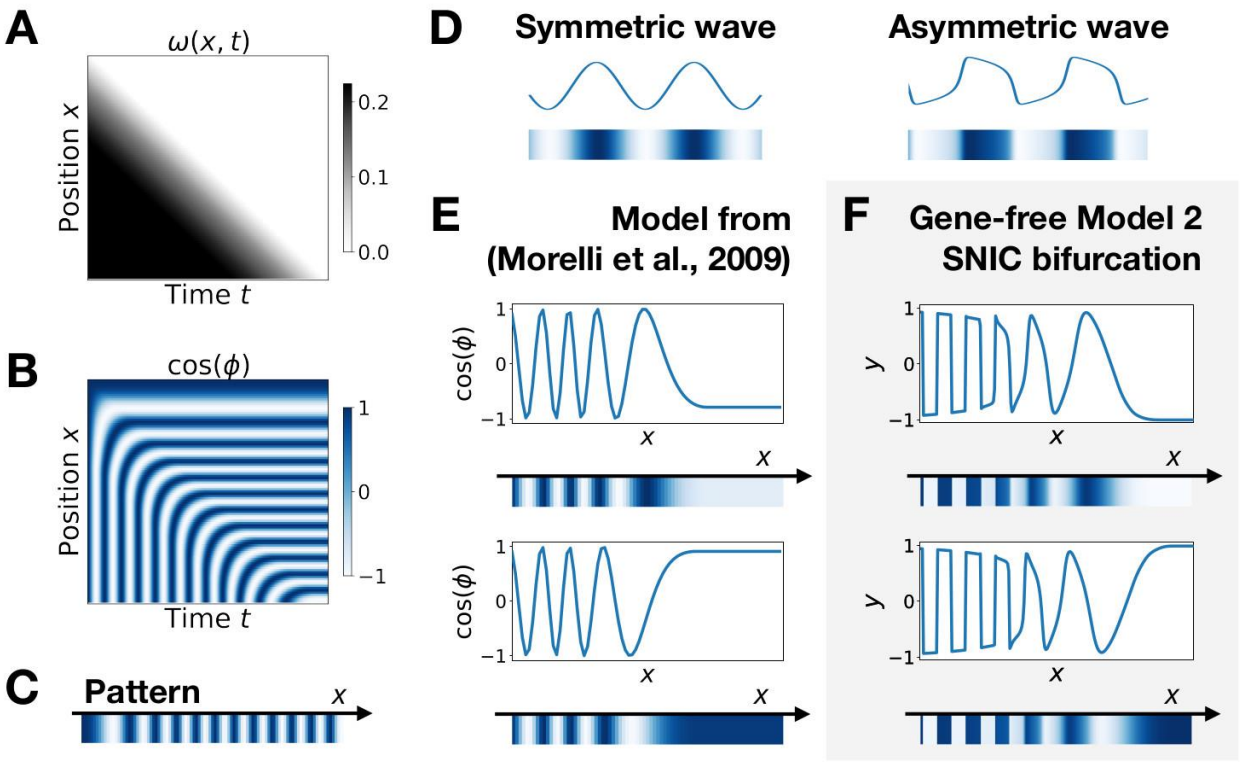

Figure 7: Wave pattern in different models for the infinite-period scenario. (*A*) Frequency profile for the simulation of the model of coupled oscillators from (Morelli et al., 2009). (*B-C*) Kymograph showing the dynamics of the phase of the oscillators and the corresponding final pattern. (*D*) Two schematic examples of possible wave patterns (symmetrical vs asymmetrical). The symmetric wave is obtained with a sine function. The asymmetric wave is retrieved from simulations of a Van der Pol oscillator. (*E*) Wave pattern for the model of Panels (*A-C*) for two different time points. (*F*) Wave pattern for Model 2 of Figure 4 for two different time points.

Supplementary Figures

Figure 1—figure supplement 1: Bifurcation analysis of the Hopf scenario of Fig. 1. (*A*) Bifurcation diagram showing the types of dynamics available to the system as a function of morphogen g concentration. The maximum and minimum concentrations of gene E on the stable limit cycle are shown in black. Stable fixed points are show in green. The main bifurcation events are identified with vertical lines. "SN" stands for saddle-node bifurcation. (*B*) Period of the oscillations along the limit cycle. (*C*) Same bifurcation diagram as in *A*, but as a function of time instead. For any given time, the diagram shows the stable fixed points and the extrema of the stable limit cycles for the concentration of morphogen g that is found in a given simulated cell at that time. The specific cell used in this diagram is the first cell of Fig. 1H.

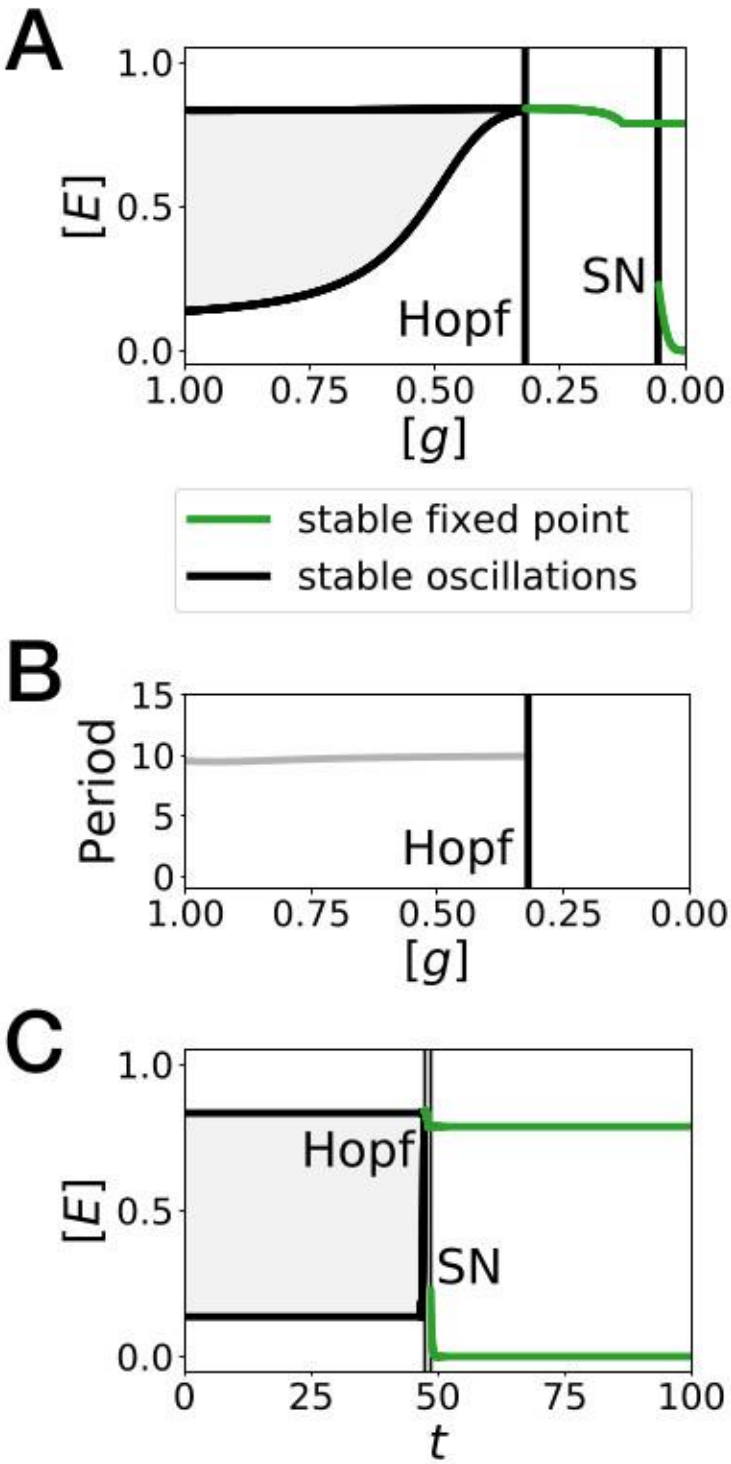

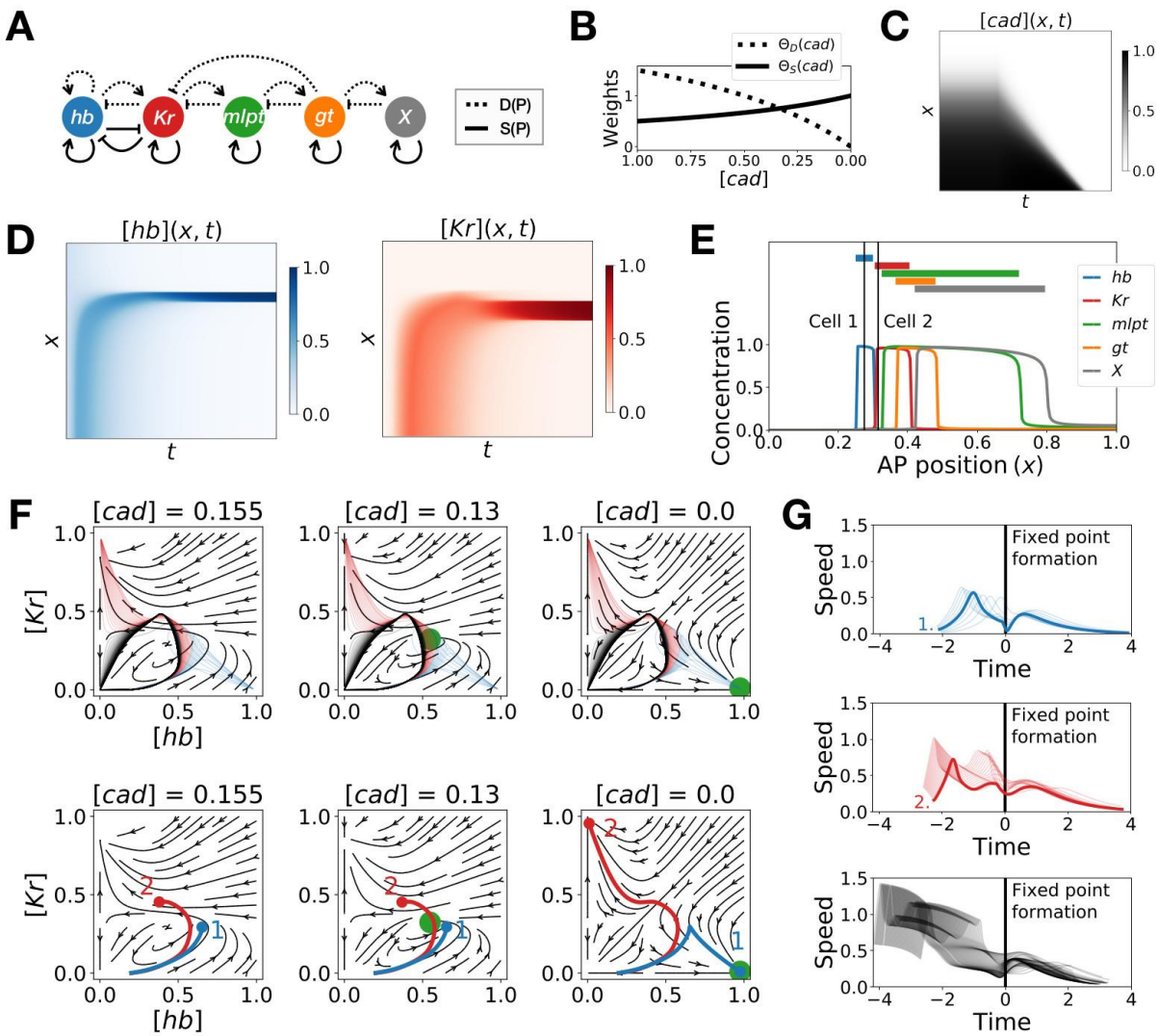

Figure 1—figure supplement 2: Two-enhancer model for *Tribolium* segmentation.

(*A*) Schematic of the gene regulatory networks encoded by the dynamic term (dotted line) and the static term (solid line). (*B*) Weights of the dynamic (dotted line) and static (solid line) enhancers. (*C*) Kymograph showing the dynamics of the concentration of morphogen *caudal* (*cad*) used in the simulated embryo. (*D*) Kymographs showing the dynamics of the concentration of proteins *hunchback* (*hb*) and *Krüppel* (*Kr*). (*E*) Final pattern of protein expression. The vertical lines identify the positions of the two cells whose trajectories are shown on the bottom subpanels of panel F. (*F*) Flow in the phase space defined by *hb* and *Kr* for different concentrations of morphogen *cad.* The green disk represents the stable fixed point corresponding to the fate with high concentration of *hb*. (*Top subpanels*) Projection of the trajectories of all cells in the *hb-Kr* phase space. The trajectories of cells that end up with high *hb*, *Kr*, and *X*

concentrations are represented with transparent blue, red and black lines, respectively. (*Bottom subpanels*) Projection of the trajectories of the two cells identified on panel E. For a given cell, the part of the trajectory that is shown is from the initial time point until the time point when *cad* reaches the concentration used to compute the flow. (G) Speed in phase space of all cells as a function of the time since the formation of the fixed point. The top, middle, and bottom subpanels show the speed of the cells that end up with high *hb*, *Kr*, and *X* concentrations at the end of the simulation, respectively. The thick blue and red lines correspond to the speed of cells 1 and 2, respectively.

Figure 2—figure supplement 1: 3-gene models for pattern formation with Hill functions for the weights. (*A*) Schematic of the gene regulatory networks encoded by the dynamic term (dotted line) and the static term (solid line). (*B*) Kymograph showing the dynamics of parameter g used in the simulated embryos for both Models 1 and 2. (*C-H*) Simulation results for Model 1. (*C*) Weights of the dynamic (dotted line) and static (solid line) enhancers as a function of parameter g. (*D*) Gene concentration and value of parameter g inside a representative simulated cell as a function of time. (*E*) Kymograph showing the dynamics of gene expression in the simulated embryo. (*F*) Schematic of the final pattern. (*G*) Bifurcation diagram showing the types of dynamics available to the simulated embryo as a function of parameter g. "SN" stands for saddle-node bifurcation. (*H*) Period (grey line) and amplitude (red line) of the oscillations along the stable limit cycle. (*I-N*) Simulation results for Model 2.

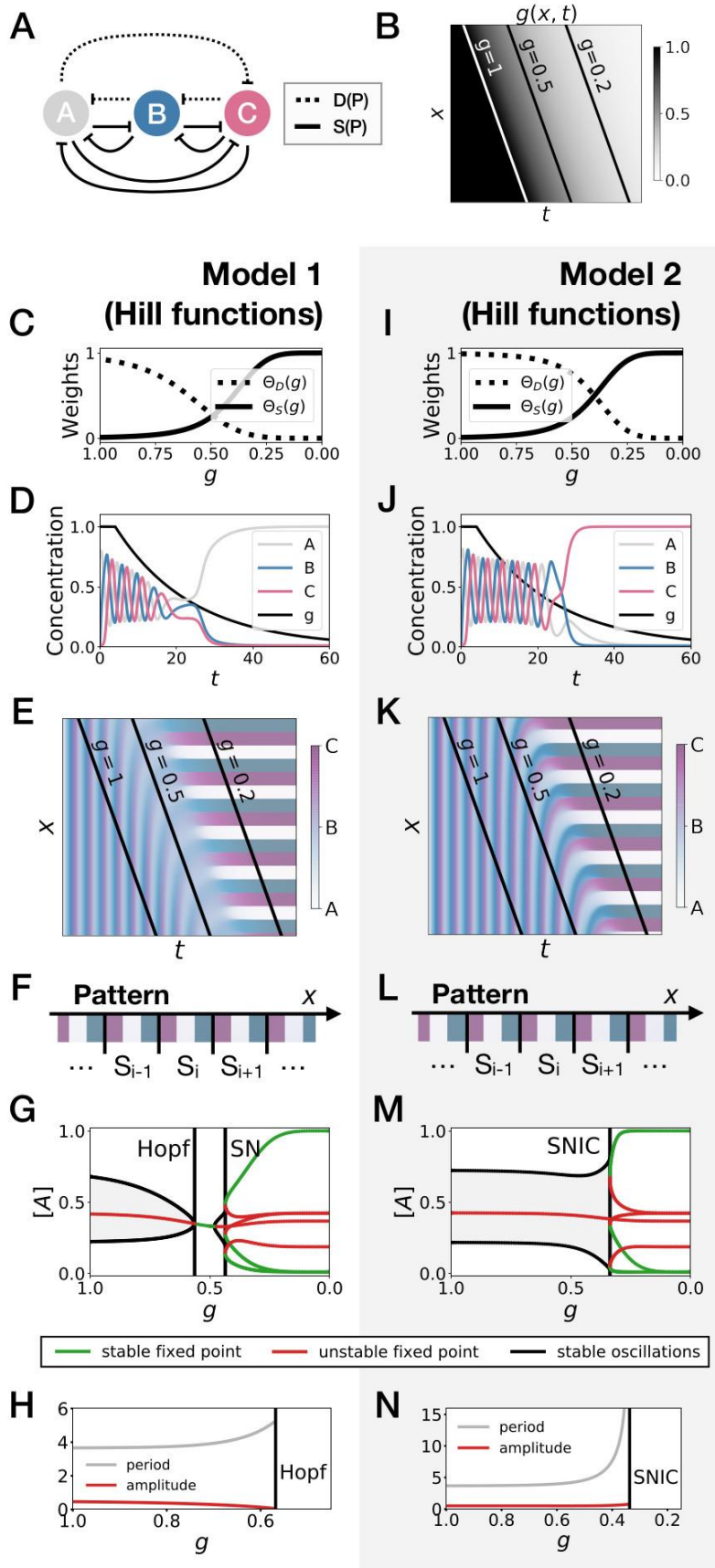

Figure 2—figure supplement 2: Peak-to-peak frequency in the 3-gene models. The red and black dots represent the normalized peak-to-peak frequency as a function of the position along the antero-posterior (AP) axis for Models 1 and 2, respectively. These data points were computed numerically by using equation 2 of (Giudicelli et al., 2007). The transparent red and black lines are the theoretical normalized frequencies of Models 1 and 2, respectively, obtained via bifurcation analysis. Note that after the Hopf bifurcation in Model 1, the system performs damped oscillations. It is therefore possible to extract a numerical peak-to-peak frequency even after the stable oscillations die during the Hopf bifurcation.

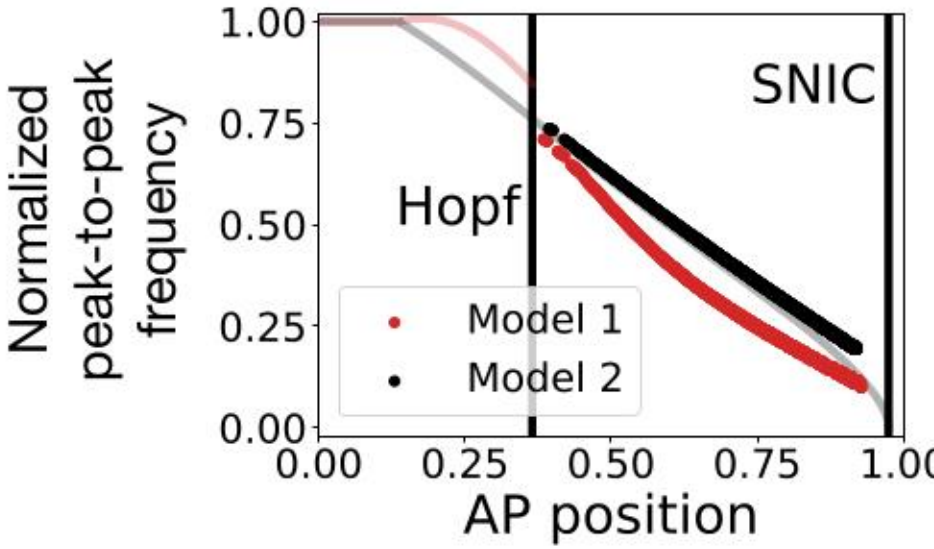

Figure 3—figure supplement 1: Stochastic simulations of the 3-gene models with Hill functions for the weights. (*A-D*) Kymographs showing the stochastic dynamics of gene expression in simulated embryos. The concentration of the three genes at the last simulated time point is shown schematically in the lower part of each panel. (*E*) Mutual information as a function of typical concentration Ω for Model 1 (red lines) and Model 2 (black lines). Paler colors correspond to lower values of the diffusion constant *D*. The thick horizontal black line indicates the ideal mutual information for three mutually exclusive genes.

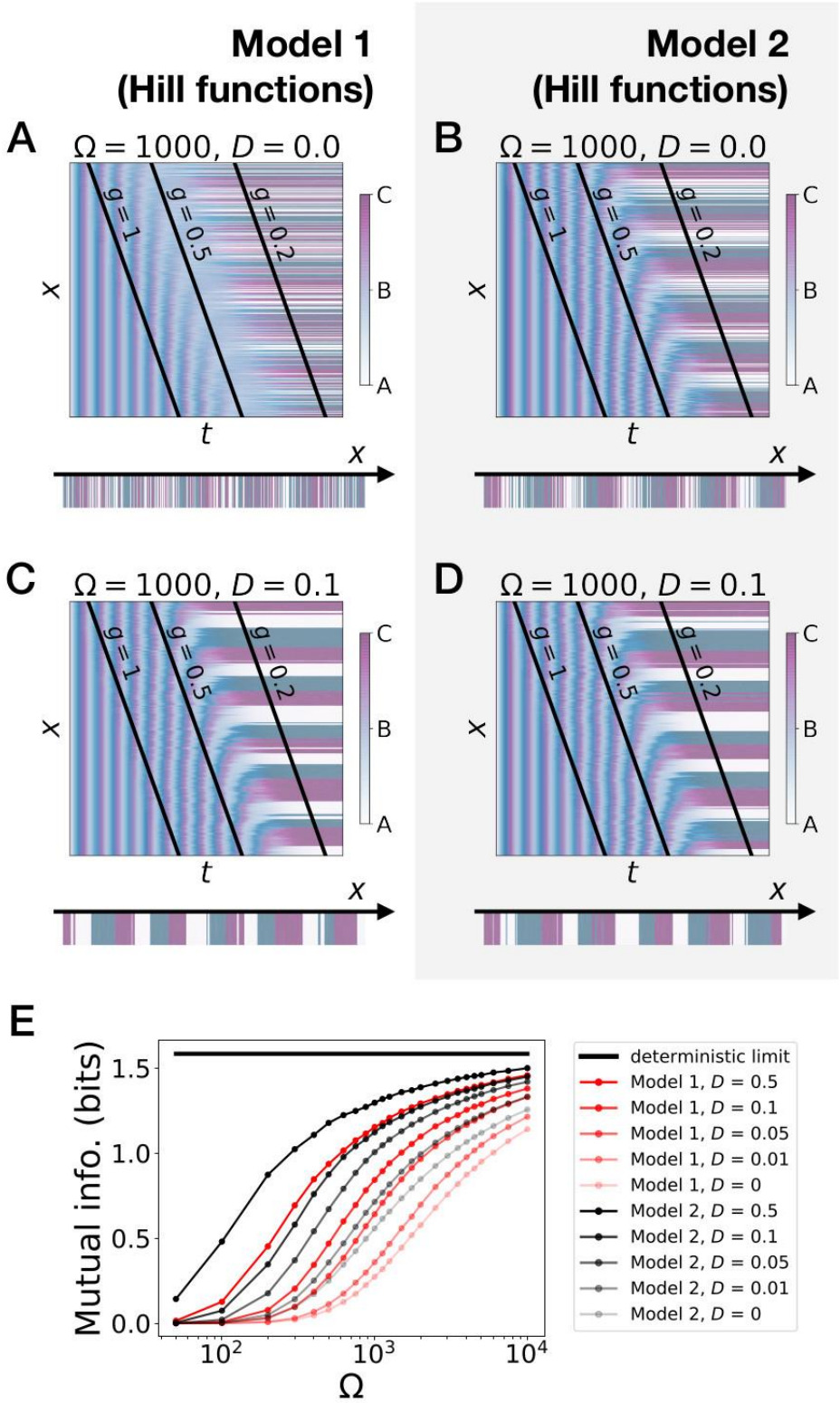

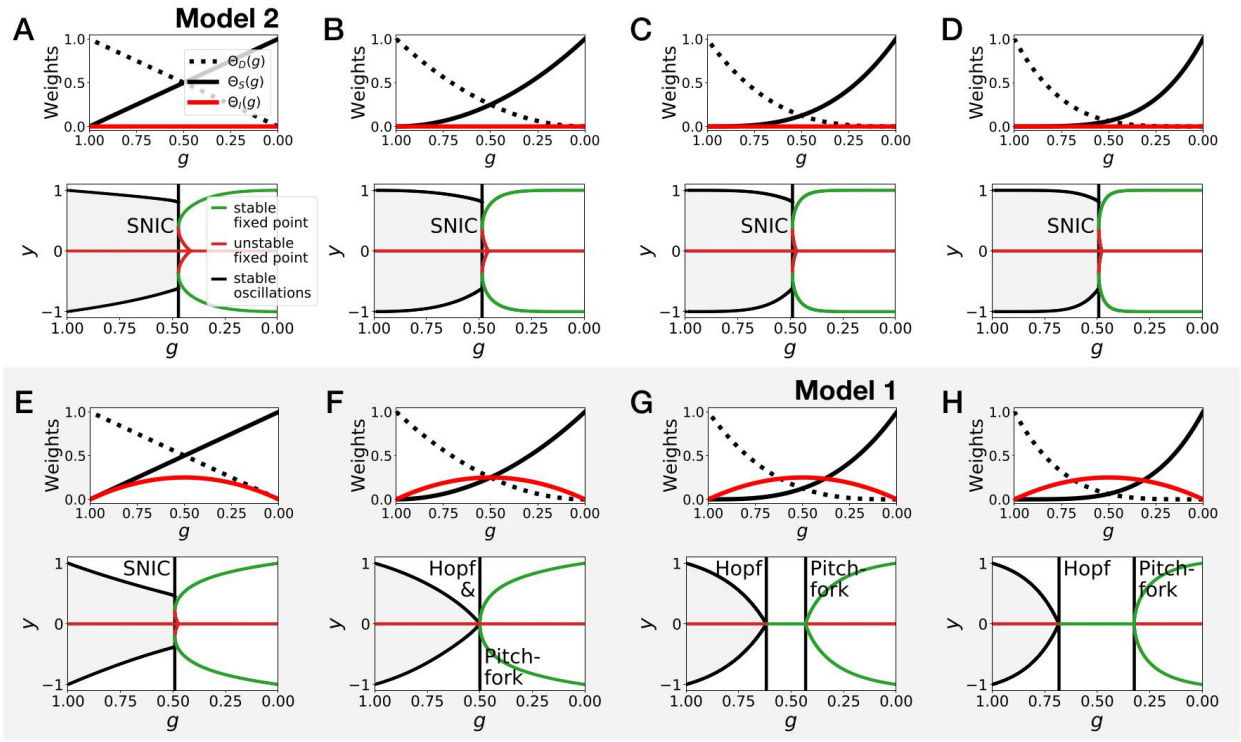

Figure 4—figure supplement 1: Gene-free models with different weights for the dynamic and static modules (*A-D*) Bifurcation analysis of gene-free models with linear weights (Model 2), quadratic weights, cubic weights and weights to the power 4. (*E-H*) Bifurcation analysis of gene-free models with linear weights, quadratic weights, cubic weights (Model 1) and weights to the power 4.

Figure 4—figure supplement 2: supercritical Hopf scenario in the gene-free model (Model 1). (*A*) Schematic of the flow encoded by the dynamic, static and intermediate terms. (*B*) Weights of the dynamic (dotted black line), static (solid black line) and intermediate (solid red line) enhancers as a function of parameter g. (*C*) Values of geometric coordinates y and z, and of parameter g in a simulated cell as a function of time. (*D*) Kymograph showing the dynamics of parameter g used in the simulated embryo. (*E*) Kymograph showing the dynamics of geometric coordinate y. (*F*) Schematic of the final pattern. (*G*) Bifurcation diagram showing the types of dynamics available to the simulated embryo as a function of parameter g. (*H*) Period (grey line) and amplitude (red line) of the oscillations. (*I*) Flow in phase space for different values of parameter g. The limit cycles are represented by thick grey lines. Positions along the limit cycle at time points separated by a fixed time interval are indicated with black dots, such that the (absence of) variations of the speed along the limit cycles can be visualized. The yellow and orange lines represent the y and z nullclines, respectively. The green and red dots represent stable and unstable fixed points, respectively.

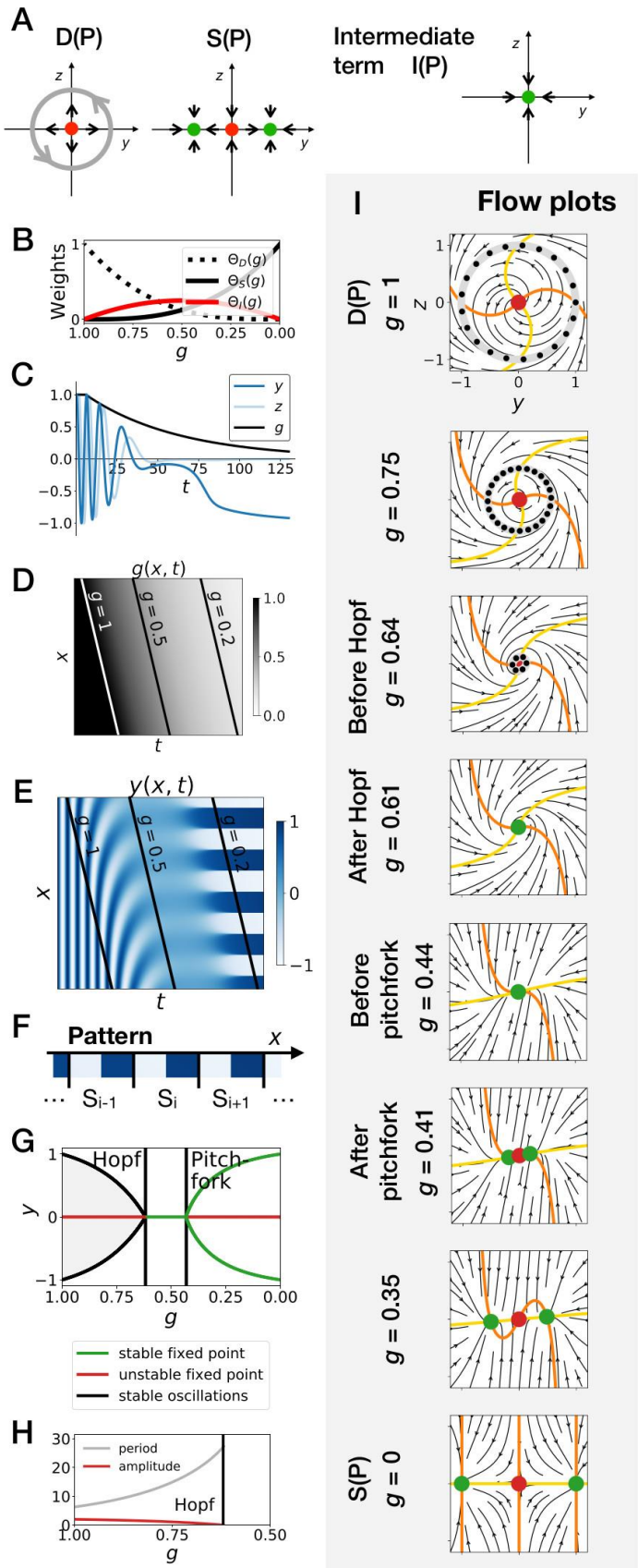

Figure 4—figure supplement 3: subcritical Hopf scenario in the gene-free model (Model 3). We can modify the dynamic module (making it more non linear) to obtain subcritical Hopf scenario (see equations in appendix) (*A*) Weights of the dynamic (dotted black line), static (solid black line) and intermediate (solid red line) enhancers as a function of parameter g. (*B*) Values of geometric coordinates y and z, and of parameter g in a simulated cell as a function of time. (*C*) Kymograph showing the dynamics of parameter g used in the simulated embryo. (*D*) Kymograph showing the dynamics of geometric coordinate y. (*E*) Schematic of the final pattern. (*F*) Bifurcation diagram showing the types of dynamics available to the simulated embryo as a function of parameter g. "SN" stands for saddle-node bifurcation. (*G*) Period (grey line) and amplitude (red line) of the oscillations. (*H*) Flow in phase space for different values of parameter g. The limit cycles are represented by thick grey lines. Positions along the limit cycle at time points separated by a fixed time interval are indicated with black dots, such that the variations of the speed along the limit cycles can be visualized. The yellow and orange lines represent the y and z nullclines, respectively. The green and red dots represent stable and unstable fixed points, respectively. "SNOLC" stands for saddle-node of limit

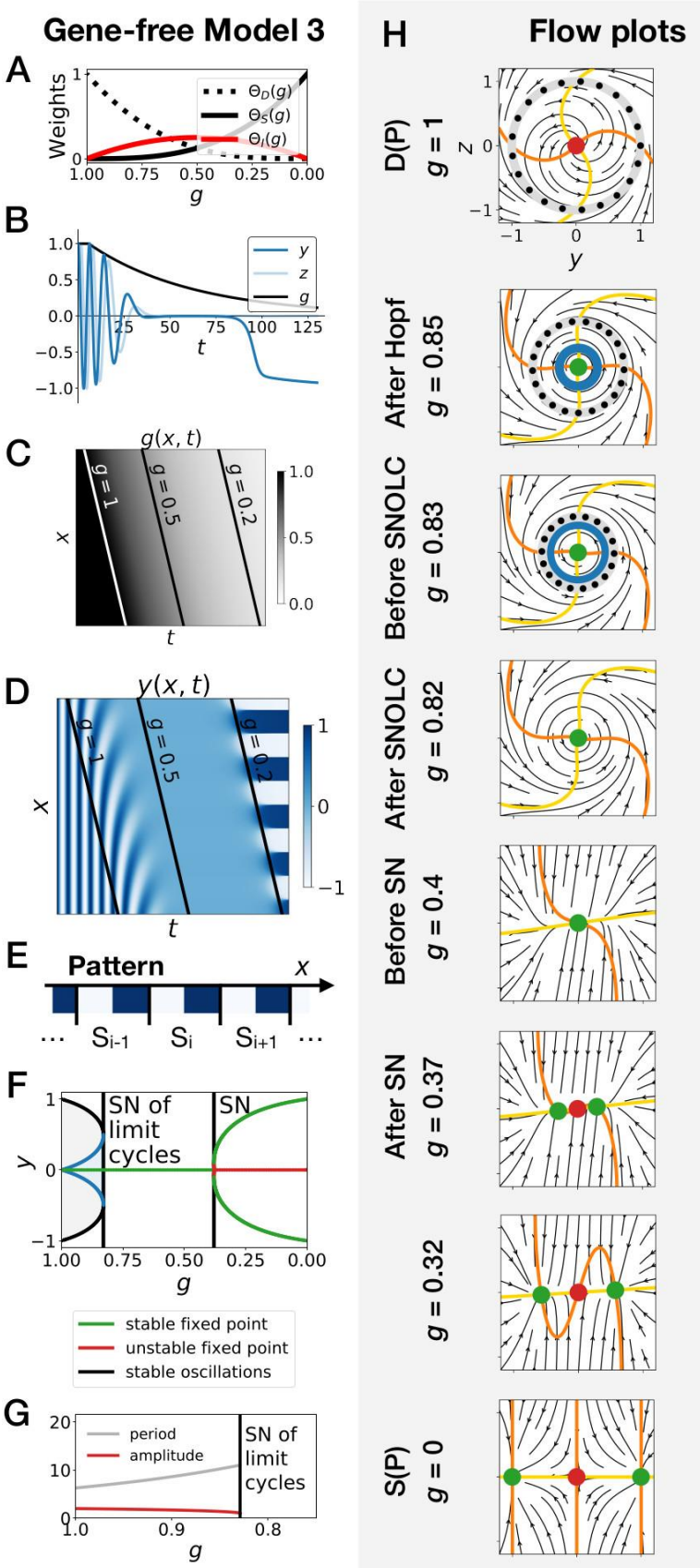

1287 cycles bifurcation.

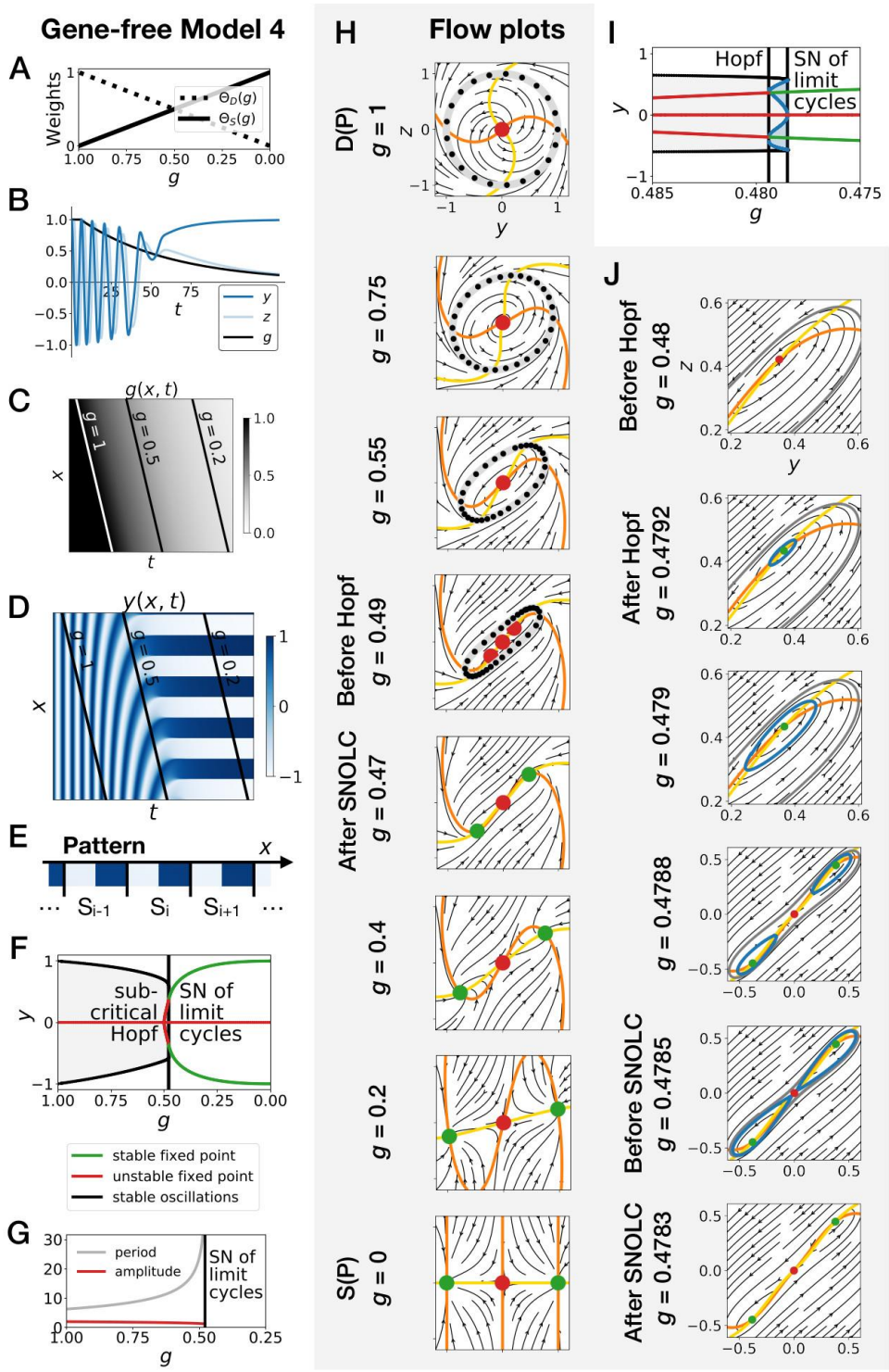

Figure 4—figure supplement 4: Gene-free model with two subcritical Hopf bifurcations (Model 4) We can modify the dynamic module (making it more non linear) to obtain

subcritical Hopf scenario (see equations in appendix) (*A*) Weights of the dynamic and static enhancers as a function of parameter g. (*B*) Values of geometric coordinates y and z, and of parameter g in a simulated cell as a function of time. (*C*) Kymograph showing the dynamics of parameter g used in the simulated embryo. (*D*) Kymograph showing the dynamics of geometric coordinate y. (*E*) Schematic of the final pattern. (*F*) Bifurcation diagram showing the types of dynamics available to the simulated embryo as a function of parameter g. "SN" stands for saddle-node bifurcation. (*G*) Period and amplitude of the oscillations. (*H*) Flow in phase space for different values of parameter g. The limit cycles are represented by thick grey lines. Positions along the limit cycle at time points separated by a fixed time interval are indicated with black dots, such that the (absence of) variations of the speed along the limit cycles can be visualized. The yellow and orange lines represent the y and z nullclines, respectively. The green and red dots represent stable and unstable fixed points, respectively. (*I*-*J*) Bifurcation diagram and flow plots for values of g close to the subcritical Hopf and saddle-node of limit cycles bifurcations. "SNOLC" stands for saddle-node of limit cycles bifurcation.

Figure 4—figure supplement 5: Stochastic simulations of the gene-free models. (*A-D*) Kymographs showing the stochastic dynamics of variable y in simulated embryos. The specific value of parameter Ω used to generate each kymograph is indicated on the panels. (*E*) Mutual information as a function of typical concentration Ω for Models 1, 2, 3 and 4. The thick horizontal black line indicates the ideal mutual information for a pattern with two symmetric regions. (*F*) Mutual information as a function of typical concentration Ω for the gene-free models of Figure 4—figure supplement 4.

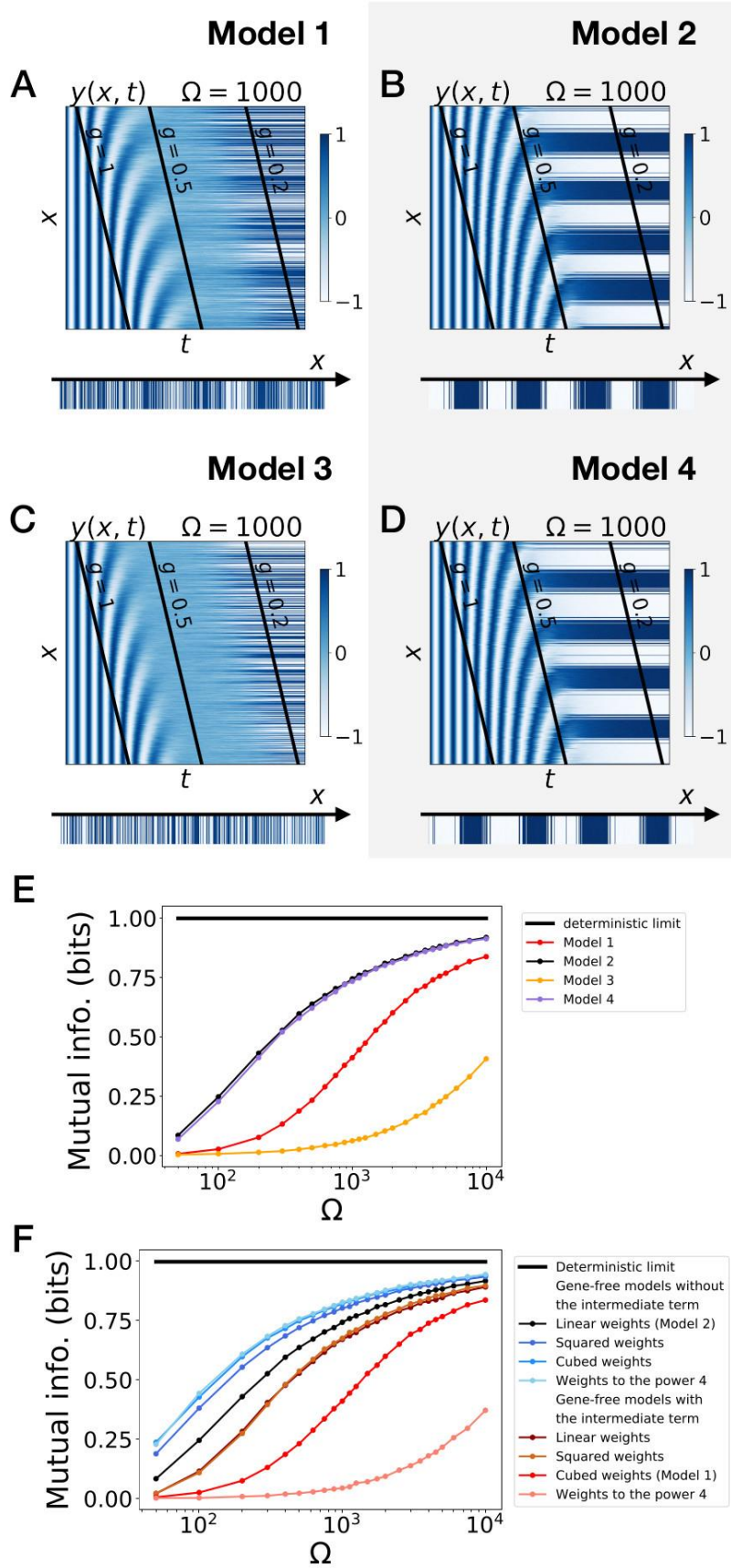

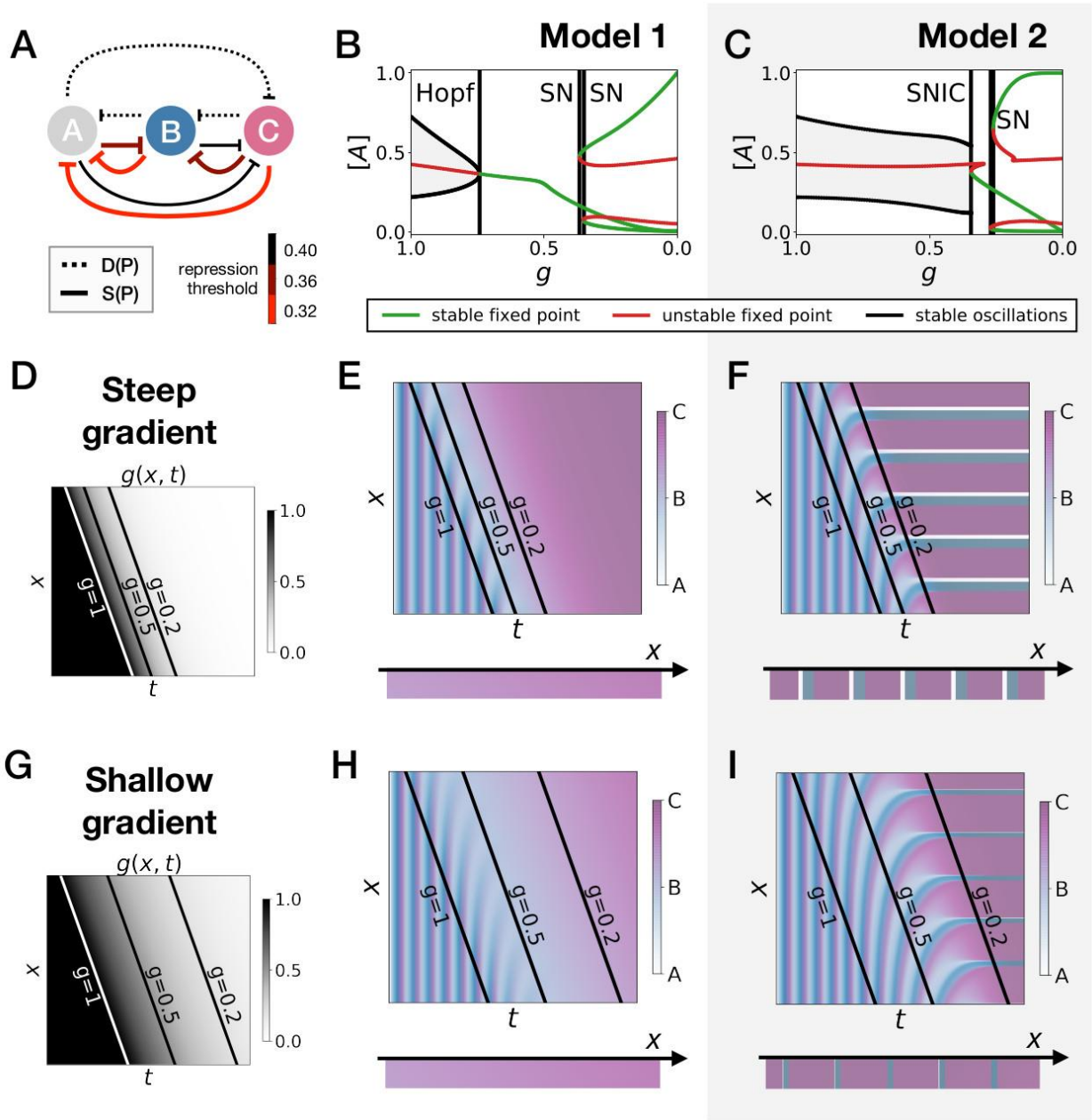

Figure 5—figure supplement 1: Perturbations of the morphogen gradient steepness in strongly asymmetric 3-gene models. (*A*) Schematic of the gene regulatory networks encoded by the dynamic (dotted line) and static (solid line) terms. For each interaction, the color indicates the strength of the repression, with darker shades of red corresponding to weaker repression. (*B-C*) Bifurcation diagram showing the types of dynamics available in Models 1 and 2. "SN" stands for saddle-node bifurcation. (*D-F*) Simulation results for a steep gradient of parameter g. (*D*) Kymograph showing the dynamics of parameter g used in the simulated embryos of both Models 1 and 2. (*E*)

Kymograph showing the dynamics of gene expression in the simulated embryos of Model 1. The concentration of the three genes at the last simulated time point is shown schematically in the lower part of the panel. (*F*) Kymograph showing the dynamics of gene expression in the simulated embryos of Model 2. (*G*-*I*) Simulation results for a shallow gradient of parameter g.

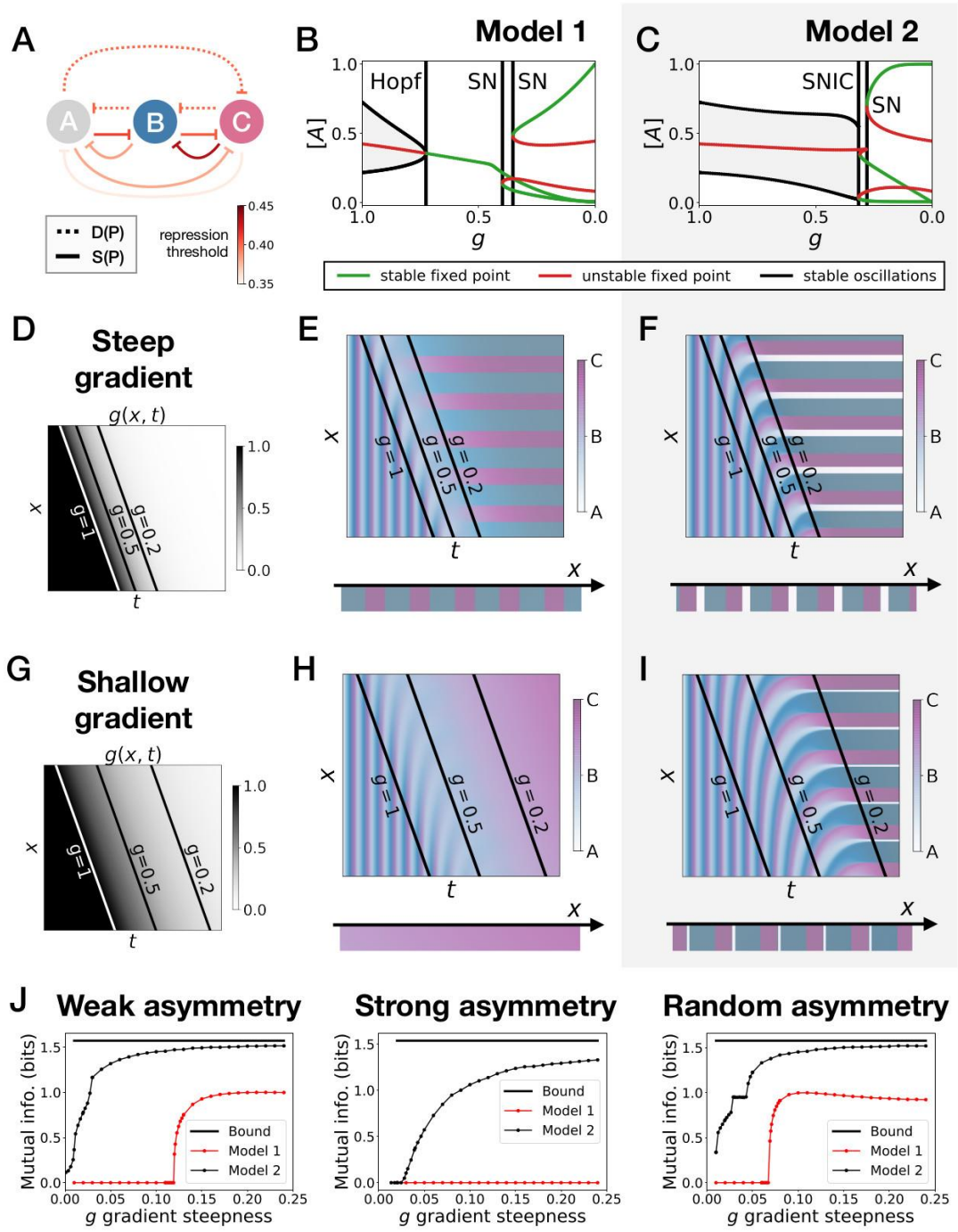

Figure 5—figure supplement 2: Perturbations of the morphogen gradient steepness in randomly asymmetric 3-gene models. (*A*) Schematic of the gene regulatory networks encoded by the dynamic (dotted line) and static (solid line) terms. For each interaction, the color indicates the strength of the repression, with darker shades of red corresponding to weaker repression. (*B-C*)

Bifurcation diagram showing the types of dynamics available in Models 1 and 2. “SN” stands for saddle-node bifurcation. (*D*-*F*) Simulation results for a steep gradient of parameter g. (*D*) Kymograph showing the dynamics of parameter g used in the simulated embryos of both Models 1 and 2. (*E*) Kymograph showing the dynamics of gene expression in the simulated embryos of Model 1. The concentration of the three genes at the last simulated time point is shown schematically in the lower part of the panel. (*F*) Kymograph showing the dynamics of gene expression in the simulated embryos of Model 2. (*G*-*I*) Simulation results for a shallow gradient of parameter g. (*J*) Mutual information as a function of the steepness of the g gradient for Models 1 (red line) and 2 (black line). The thick horizontal black line indicates the theoretical upper bound. The left, center and right subpanels show respectively the mutual information for models with a weak asymmetry in the fixed points of the static term (Fig. 5), with a strong asymmetry (Supp. Fig. 7) and with a random asymmetry (this figure).

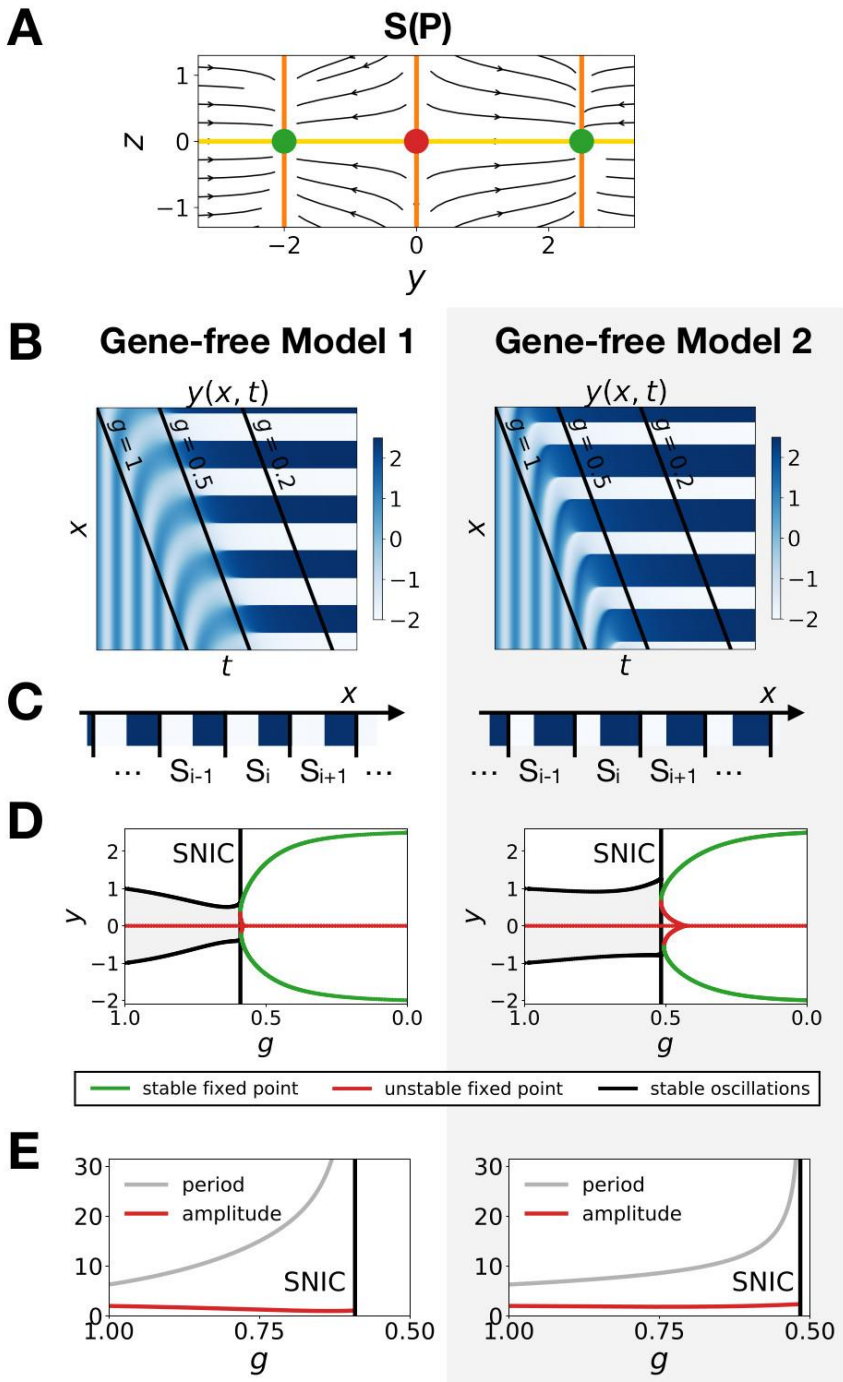

Figure 6—figure supplement 1: Model 1 becomes a SNIC when fixed points are outside the limit cycle. (*A*) Flow plots showing the change of geometry of the static module. (*B-C*) Corresponding kymographs and final patterns for Models 1 and 2. (*D-E*) Associated bifurcations diagrams and plots of the period and amplitude of the oscillations as a function of parameter g.

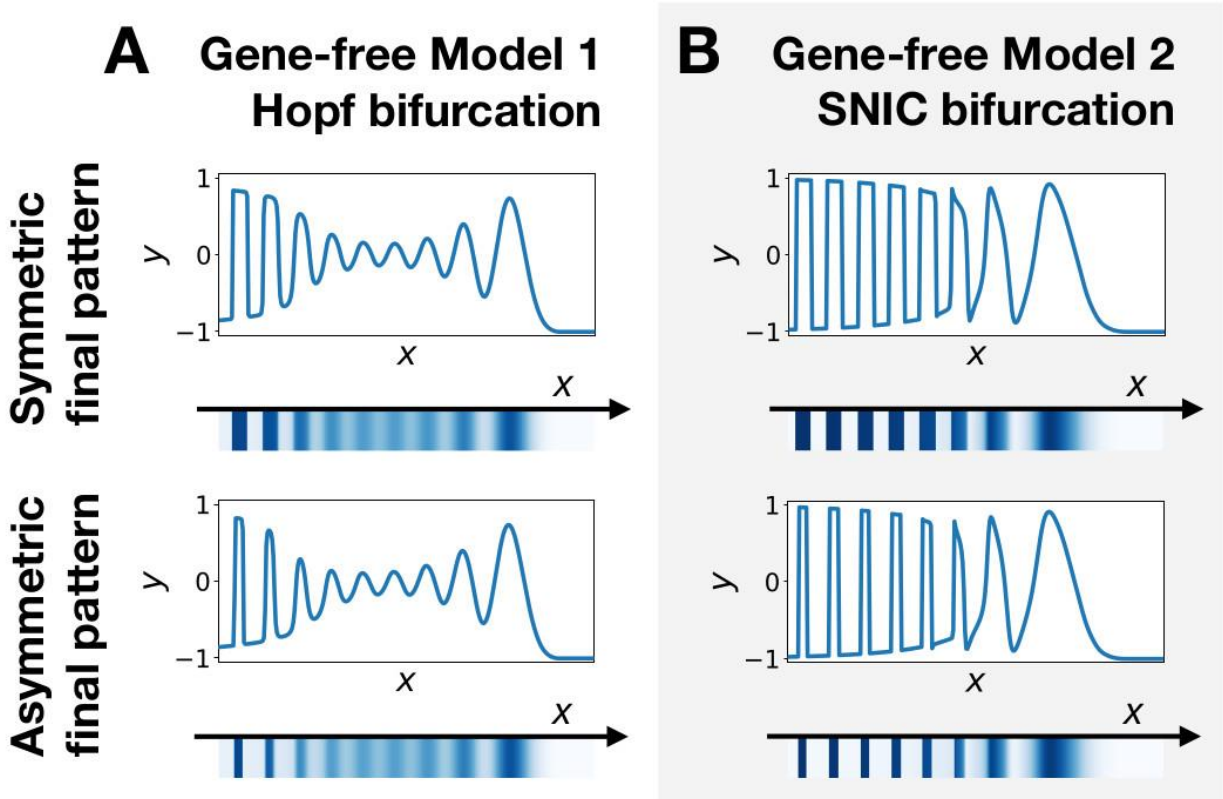

Figure 7—figure supplement 1: Wave pattern in different versions of the 2D gene-free model. (*A*) Wave patterns of the gene-free Model 1 with a Hopf bifurcation. The top and bottom subpanels show the wave pattern for symmetric and asymmetric fixed points in the static term, respectively. (*B*) Wave patterns of the gene-free Model 2 with a SNIC bifurcation.

Figure 7—figure supplement 2: Distribution of the values of the geometric variables (gene-free models) and of the gene concentrations (3-gene models). (*A*) Histograms showing the distributions of the values of the y (dark blue) and z (light blue) variables in gene-free Models 1, 2, 3 and 4 for different values of parameter g. (*B*) Histograms showing the distributions of the concentrations of genes A (grey), B (blue) and C (pink) in 3-gene Models 1 and 2 for different values of parameter g.

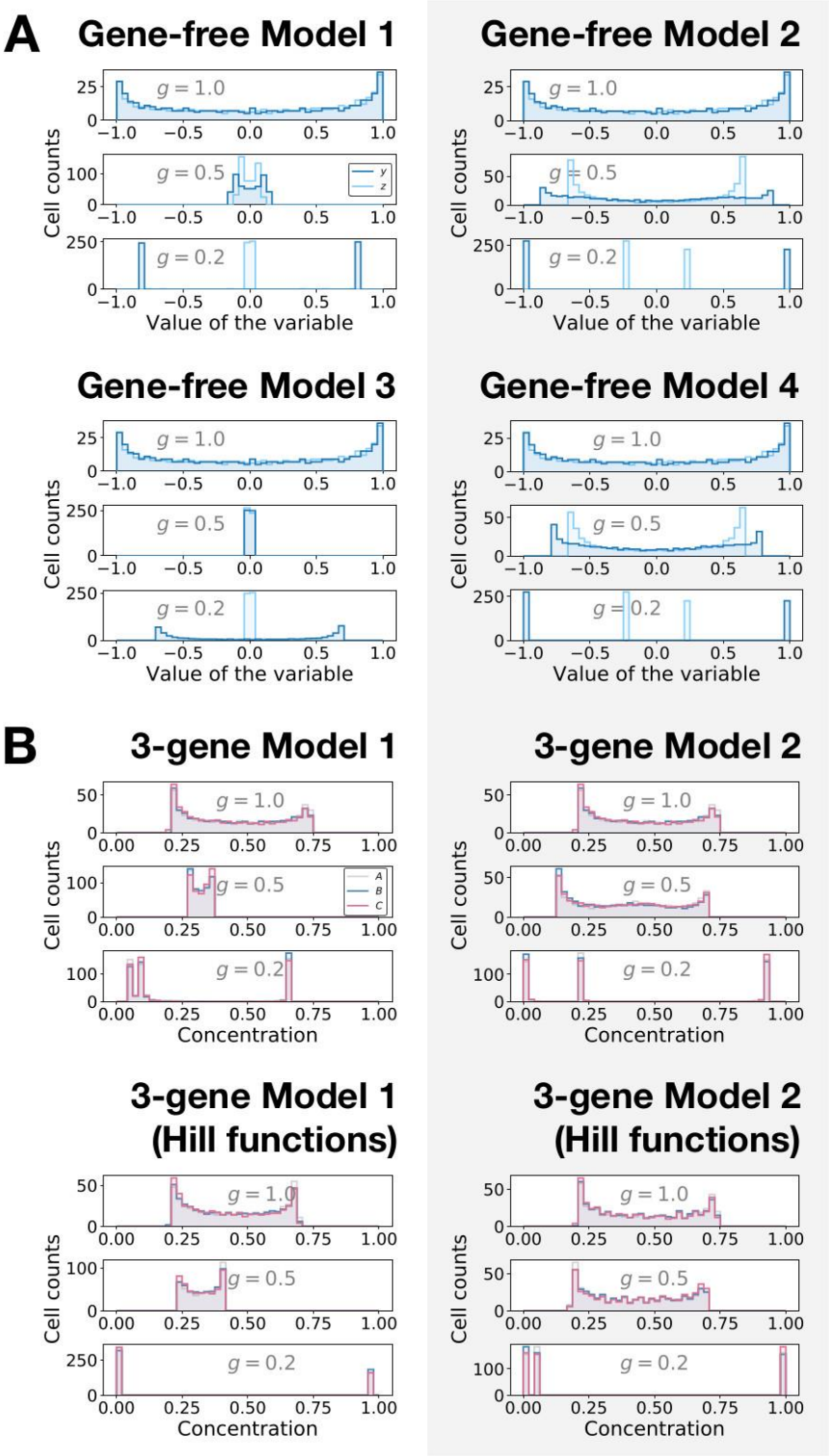

Supplementary Movie Legends

Figure 4—video 1: Flow of the gene-free with a supercritical Hopf bifurcation (Model 1). Flow in phase space as parameter g goes from 1 to 0. The stable limit cycles are represented by thick grey lines. The yellow and orange lines represent the y and z nullclines, respectively. The green and red dots represent stable and unstable fixed points, respectively.

Figure 4— video 2: Flow of the gene-free with a SNIC bifurcation (Model 2). Flow in phase space as parameter g goes from 1 to 0. The stable limit cycles are represented by thick grey lines. The yellow and orange lines represent the y and z nullclines, respectively. The green and red dots represent stable and unstable fixed points, respectively.

Figure 4— video 3: Flow of the gene-free with a subcritical Hopf bifurcation (Model 3). Flow in phase space as parameter g goes from 1 to 0. The stable and unstable limit cycles are represented by thick grey and blue lines, respectively. The yellow and orange lines represent the y and z nullclines, respectively. The green and red dots represent stable and unstable fixed points, respectively.

Figure 4— video 4: Flow of the gene-free with two subcritical Hopf bifurcations (Model 4). Flow in phase space as parameter g goes from 1 to 0. The stable limit cycles

are represented by thick grey lines. The yellow and orange lines represent the y and z nullclines, respectively. The green and red dots represent stable and unstable fixed points, respectively.

Figure 7— video 1: Comparison of pattern formation dynamics in different models. Dynamics of the spatial wave patterns in four models: a phase model with diverging period similar to the infinite-period scenario of Figure 1, the symmetric gene-free Model 1, the symmetric gene-free Model 2, and the asymmetric gene-free Model 2.